# THE TURBULENT REACTING RICHTMYER-MESHKOV INSTABILITY: A NEW CANONICAL PROBLEM IN NON-PREMIXED COMBUSTION

by

Hilda Varshochi

A dissertation submitted to the faculty of
The University of North Carolina at Charlotte
in partial fulfillment of the requirements
for the degree of Doctor of Philosophy in
Mechanical Engineering

Charlotte

2016

Approved by:

_____
Dr. Praveen Ramaprabhu

_____
Dr. Russell Keanini

_____
Dr. Wei Cai

_____
Dr. Mohammad Kazemi

# ABSTRACT

HILDA VARSHOCHI. The turbulent reacting Richtmyer-Meshkov Instability: A new canonical problem in non-premixed combustion. (Under the direction of DR. PRAVEEN RAMAPRABHU)

We describe detailed high-resolution numerical simulations of a class of shock-induced reactive turbulent mixing layers, where the scalar mixing, flow dynamics and combustion properties are driven by the Richtmyer-Meshkov (RM) instability. The 3D high-resolution, numerical simulations of a reacting RM turbulent mixing layer were performed with the astrophysical FLASH code, with modifications to describe chemical reactions and heat release relevant to combustion applications. In the numerical simulations, a Mach 1.58 shock traverses a diffuse, corrugated material interface separating Hydrogen at 1000 K and Oxygen at 300 K, so that local misalignments between pressure and density gradients induce baroclinic vorticity at the contact line. We study the evolution of the interface and the flame as the resulting RM instability grows through linear, nonlinear and turbulent stages. We develop a detailed understanding of the effects of heat release and combustion on the underlying flow properties by comparing our results with a baseline non-reacting RM flow. The shock-driven instability growth enhances mixing at the interface, thus creating the conditions for efficient burning at the flame site. Conversely, the presence of the flame has a profound effect on the instability growth rates through the action of associated combustion waves and heat release at the site of burning. We document the properties of the instability (growth rates, molecular mixing fraction) and the flame (fluctuations of mixture fraction, temperature, scalar dissipation rate) as well as the nature of the coupling between the two. We find the

incident shock energizes the flow, increases the scalar dissipation rate, while decreasing the Damkohler number. In contrast, the subsequent nonlinear decay of the instability is accompanied by an increase in the Damkohler number. We provide simple models that link the scalar dissipation rate and other flame-critical quantities to easily measured RM instability properties such as the integral mix width and the molecular mixing parameter. Our findings are relevant to supernovae detonation, knocking in IC engines and scramjet performance, while the underlying flow problem defined here represents a novel canonical framework to understand the broader class of non-premixed turbulent flames.

# DEDICATION

I dedicate my dissertation to my dear father and the memory of my beloved mother, who dedicated their lives to my sisters and I.

Also, I dedicate this thesis to all readers.

# ACKNOWLEDGMENTS

My research would not have been possible, if I did not get encouragement and support from a number of people. Their words and suggestions often boosted my courage and determination. I would like to thank my graduate advisor, Dr. Praveen Ramaprabhu, who trusted me and gave me the opportunity to work on this complex filed of research. He was always accessible and his perpetual energy and enthusiasm in research motivated me. I would like to thank my committee members Dr. Russell Keanini, Dr. Wei Cai and Dr. Mohammad Kazemi for spending their valuable time in reviewing my dissertation. I would like to acknowledge the Flash center at the University of Chicago for providing access to the FLASH code. FLASH was developed by the FLASH center at U. Chicago with support from DOE NNSA-ASC OASCR.

TABLE OF CONTENTS

LIST OF FIGURES

# LIST OF TABLES

# NOMENCLATURE

| | |
|---|---|
| $At$ | Atwood number |
| $\gamma_i$ | Adiabatic index of species $i$ |
| $\tau_c$ | Chemical reaction time scale |
| $h_b$ | Amplitude of bubble |
| $h_s$ | Amplitude of spike |
| $\Gamma$ | Circulation |
| $Da$ | Damkohler number |
| $h_0$ | Initial amplitude of bubble and spike accumulated |
| $I$ | Intensity of segregation |
| $\Delta U$ | Interface jump velocity |
| $\eta$ | Kolmogorov length scale |
| $Y_i$ | Mass fraction of species $i$ |
| $\tau_f$ | Mixing time scale |
| $W$ | Mixing width |
| $Z$ | Mixture fraction |
| $z'$ | Mixture fraction fluctuations on a plane |
| $\Theta$ | Molecular mixing fraction |
| $\theta$ | Power-law exponent |
| $A$ | Pre-exponential factor in power-law method |
| $Re$ | Reynolds number |

$\sqrt{u'^2}$ rms of turbulent velocity fluctuations in X direction

$\sqrt{v'^2}$ rms of turbulent velocity fluctuations in Y direction

$\sqrt{w'^2}$ rms of turbulent velocity fluctuations in Z direction

$\chi$ Scalar dissipation rate

$\tau_s$ Scalar dissipation time scale

$\xi$ Scaled x coordinate

$Z_{st}$ Stoichiometric mixture fraction

$\chi_{st}$ Stoichiometric scalar dissipation rate

$E$ Total energy

$\varepsilon$ Turbulent dissipation rate

$\tau_t$ Turbulent dissipation time scale

$tke$ Turbulent kinetic energy

$\vec{\omega}$ Vorticity vector

$k$ Wave number

## AVERAGING METHODS

$<*>$ Planar average

$\{*\}$ Average of quantity on an iso-surface

$\bar{*}$ Time average

# CHAPTER 1: INTRODUCTION

The Richtmyer-Meshkov (RM) instability refers to the unbounded growth of perturbations at a material interface between different gases, when such an interface is impulsively accelerated [1-3]. The impulsive acceleration could be provided by an incident shock, such that the perturbation growth is driven by the deposition of baroclinic vorticity at the interface due to local misalignments between the shock and the interface [4-6]. As a result, the ensuing perturbation growth proceeds through linear[1,7] , nonlinear [8,9], and turbulent [10] stages. The eventual turbulent state in such flows may either be profoundly detrimental to design objectives in applications such as Inertial Confinement Fusion [11], or if properly manipulated could benefit the performance of devices such as Scramjet engines [12]. In the latter application, the instability-driven turbulent mixing between fuel and oxidizer streams can be rate-limiting to the combustion process. Thus, the flow affects the flame and vice-versa. In his review of turbulent mixing, Dimotakis [12,13] proposed a hierarchy of mixing processes extending from passive scalar (Level 1) to so-called Level 3 mixing, where the flow dynamics and active scalar mixing are intimately coupled. Such a direct coupling between flow and non-premixed flame dynamics suggests two opportunities: (i) In a carefully defined problem configuration, essential flame properties may be characterized in terms of RM

flow properties which are easier to measure without the use of expensive laser diagnostics. Such an understanding can point the way to the design of experiments in which measurements of integral quantities such as the turbulent mixing width may be related to combustion properties. (ii) Insights in to the coupling between flame and flow characteristics in the context of non-premixed RM combustion can lead to control strategies that achieve a desired combustion state by employing 'designer' initial conditions. In this work, we tackle the first issue by defining and studying a novel RM flame configuration, which we believe will lead to insights in to the broader class of turbulent, non-premixed flames.

The role of RM-driven mixing in shaping the evolution of a spherical flame bubble has been investigated extensively through experiments and numerical simulations. Early efforts include the experiments of Markstein [14] who investigated the interaction of a planar incident shock with a spherical flame bubble. The experiments suggested a link between the baroclinic vorticity deposition from shock impact and the subsequent development of a chaotic flame through instability. RM-driven mixing was investigated theoretically by Picone [6] in the context of shock interaction with a cylindrical flame region. The problem has also received attention in several numerical studies including the study of shock-flamelet interactions [15-17], shock interactions with cylindrical jet flames [18], and DDT in shock-bubble configurations [19]. Haehn et al.[20] reported results from an experimental study in which an incident shockwave is focused by a spherical bubble containing a premixed composition of $H_2$, $O_2$ and Xe. The shock focusing by the spherical gas lens creates a local hot spot that triggers ignition, followed by burning that envelopes the bubble region. While these efforts have led to significant

insight into the interaction of a planar shock with a cylindrical or spherical flame/bubble, they represent an idealization of RM-driven combustion in applications which predominantly feature a material interface subjected to random perturbations. The requirement to model controlled initial perturbations has led to recent numerical simulation studies in which shocks accelerate planar premixed flames subjected to well-defined initial conditions. For instance, Khokhlov et al. [21] investigated the growth of a sinusoidally perturbed, premixed flame upon shock impingement, and found the energy release from combustion scaled with the RM driven interfacial surface growth. In this work, we have explored for the first time the relationship between RM-driven flow properties and flame characteristics in a non-premixed setting with well-defined initial conditions – a flat interface with imposed perturbations.

Thus, our objectives in this work are threefold: 1- To investigate the effect of reactions on RM integral quantities such as mixing width and molecular mixing parameter, 2- To evaluate the self-similarity of turbulent flow under the influence of combustion heat release 3- To propose simple models to estimate turbulent flow quantities (such as mixture fraction and mean scalar dissipation rate) purely in terms of RM integral parameters.

We briefly review the phenomenology of non-reacting RM, before a detailed discussion of its reacting counterpart that is the centerpiece of this work. When a sharp interface between different gases is impulsively accelerated by a shock, perturbations of wavelength λ and initial amplitude $h_0$ will grow according to

$$\dot{h}_0 = k\Delta U\, Ah, \qquad (1.1)$$

where $At = \frac{\rho_2 - \rho_1}{\rho_2 + \rho_1}$ is the Atwood number characterizing the density discrepancy between the gases and ΔU is the jump velocity acquired by the interface as a result of the shock contact. Equation (1.1) was obtained by treating the acceleration from the shock as an impulse function [1], and integrating the resulting perturbation equations. However, the applicability of the so-called impulsive model is limited by two factors: Eq. (1.1) is valid only in the limit of weak shocks and vanishingly small perturbations. The former shortfall was addressed by Richtmyer [1] himself by numerically solving the linearized hydrodynamic equations. The latter concern implicates many RM experiments [2,22-26], since they typically violate $kh_0 \ll 1$ where $k = \frac{2\pi}{\lambda}$ is the wavenumber of imposed perturbations.

When large initial amplitudes are present at the interface, the peak growth rate is a fraction of the prediction from eq. (1.1) (or the more extensive linear theory). Furthermore, at large A perturbations become asymmetric, so that it is useful to differentiate bubbles of light fluid penetrating the heavy, from spikes of the heavy fluid traveling in the opposite direction. Several models have been proposed to describe the growth rate attenuation due to nonlinearity [27,28], with varying degrees of success in predicting experimental/simulation results. When a spectrum of modes is present at the initial interface, the flow evolves in to turbulence through a combination of bubble competition and merger mechanisms [29,30]. The resulting flow is self-similar, while there is strong evidence the aggregate mixing width follows the power law:

$$W = W_0(t - t_0)^{\theta}. \qquad (1.2)$$

Experiments [31] and numerical simulations [32] suggest the power law exponent depends weakly on the Atwood number, and varies from 0.1 to 1.

The rest of this document is structured as follows: In chapter 2, we describe the problem configuration investigated here and provide the details of the numerical techniques employed. We provide insight to RMI driven non-premixed combustion by analyzing results of two simple configurations in chapter 3. Turbulent flow properties in RM driven flows are presented in chapter 4. Chapter 5 section 1 is a discussion of 1D flame dynamics, while the self-similar behavior of non-premixed RM flames is discussed in § 5.2. The effect of flame presence on the evolution of the turbulent RM mixing layer is presented in § 5.3. We continue chapter 5 by proving power-law analysis of mixing width in 5.4 and a discussion on molecular mixing width and intensity of segregation in 5.5. In chapter 6, we propose a simple model for mixture fraction variances $z''^2$, and mean scalar dissipation rate ($\chi$) in terms of RM integral quantities. Lastly, some concluding thoughts are presented in chapter7.

# CHAPTER 2: NUMERICAL METHODS AND PROBLEM SETUP

In this chapter we briefly describe the FLASH code along with capabilities relevant to the problem studied here. We also describe the problem configuration, initial conditions and boundary conditions employed.

## 2.1 FLASH Code Description

The simulations described in this work were performed using the massively parallel astrophysical FLASH code [33,34], with modifications by Attal et al. [35] that included several capabilities relevant to the description of combustion applications. FLASH uses the directionally split, Piecewise Parabolic Method (PPM) [36], to solve the compressible Euler equations. The Equation of State (EOS) unit in FLASH was modified [35] to handle multiple species, each with temperature-dependent properties, and can be invoked in three distinct modes using different pairs of thermodynamic input properties: density-temperature, density-pressure and, density-internal energy.

## 2.2 Hydrodynamics Unite:

The compressible Euler equations (2.1) – (2.3) are solved in the Hydro unit [33]:

$$\frac{d\rho}{dt} + \nabla.(\rho V) = 0, \tag{2.1}$$

$$\frac{d\rho V}{dt} + \nabla.(\rho VV) + \nabla P = \rho g, \tag{2.2}$$

$$\frac{d\rho E}{dt} + \nabla.[(\rho E + P)V] = \rho V.g \tag{2.3}$$

where $g$, $\rho$, $V$, $P$ and $E$ are the gravitational acceleration, density, velocity, pressure and the total energy per unit mass, respectively. The internal energy ($e$) is obtained separately from equation (2.4),

$$\frac{d\rho e}{dt} + \nabla.[(\rho e + P)V] - V.\nabla P = 0. \tag{2.4}$$

In multi species mixtures, conservation equation (2.5) is applied on each species.

$$\frac{\partial \rho Y_i}{\partial t} + \nabla.(\rho Y_i V) = 0 \tag{2.5}$$

where $Y_i$ is the mass fraction of the $i^{th}$ species.

Finally, pressure is computed using an ideal gas equation of state (§ 2.3).

The matrix of Euler equations, is handled and solved using directionally split Piecewise Parabolic Method (PPM) [36] in FLASH. PPM is an extension to second order of the first order Godunov method [37].

## 2.3 Equation of State (EOS) Unit

For the simulations reported herein, the EOS unit was invoked in density-pressure mode, so that the temperature of the mixture is computed first based on the mixture molecular weight using the equation:

$$T = \frac{A_{avg}P}{R\rho}, \tag{2.6}$$

where $R$ is the universal gas constant and $A_{avg}$ is the mixture's average atomic mass. $A_{avg}$ is calculated from each species atomic mass $A_i$ and mole fraction $Y_i$ according to:

$$\frac{1}{A_{avg}} = \sum_i \frac{Y_i}{A_i}, \tag{2.7}$$

where, subscript $i$ stands for individual species. The adiabatic index of each species is then calculated as a function of temperature [38]:

$$\frac{C_{p_i}}{R} = a_1 + a_2 T + a_3 T^2 + a_4 T^3 + a_5 T^4 \, , T > 1000\ K \tag{2.8-a}$$

$$\frac{C_{p_i}}{R} = a_8 + a_9 T + a_{10} T^2 + a_{11} T^3 + a_{12} T^4 \, , T > 1000\ K \tag{2.8-b}$$

where $a_8 - a_8$ are thermodynamic polynomial coefficients of species $i$ [38]

The mixture adiabatic index is calculated according to:

$$\gamma_{avg} = 1 + \left( W_{avg} \sum_i^N W_i \frac{Y_i}{\gamma_i - 1} \right)^{-1}, \tag{2.9}$$

where $W_i$, $Y_i$ and, $\gamma_i$ are the molecular weight, mass fraction and adiabatic index of each species, while $M_{avg}$ is the average molecular weight of the mixture. Finally, the internal energy is computed using the following equation:

$$e = \frac{RT}{A_{avg}(1 - \gamma_{avg})}. \tag{2.10}$$

## 2.4 Viscosity and Thermal Conductivity

The diffusion of mass, momentum and heat are captured in FLASH through associated fluxes imposed on the cell boundaries. The flux-based diffusion solver is an indirect method to account for diffusion effects, that does not operate on the primary variables, instead updating the fluxes due to diffusion heat, mass and momentum [33].

We implement the semi empirical method presented by Wilke [39] to compute viscosity of the gas mixture, $\mu_{mix}$, as shown in eq. (2.11):

$$\mu_{mix} = \sum_{i=1}^{N} \frac{\mu_i X_i}{\sum_{j=1}^{N} X_i \, \Phi_{ij}} \tag{2.11-a}$$

and

$$\Phi_{ij} = \frac{1}{\sqrt{8}} \left(1 + \frac{A_i}{A_j}\right)^{-\frac{1}{2}} \left(1 + \left(\frac{\mu_i}{\mu_j}\right)^{\frac{1}{2}} \left(\frac{A_i}{A_j}\right)^{\frac{1}{4}}\right)^2, \tag{2.11-b}$$

where dynamic viscosity of each species, $\mu_i$, is determined as a function of temperature in the form of a polynomial curve fit with 8 coefficients [40]:

$$ln\ _i = b_1 ln\, T + \frac{b_2}{T} + \frac{b_3}{T^2} + b_4,\ T > 1000K \tag{2.12-a}$$

$$ln\mu_i = b_5 ln\, T + \frac{b_6}{T} + \frac{b_7}{T^2} + b_8,\ T < 1000K. \tag{2.12-b}$$

In the same manner, thermal diffusivity of pure elements is computed from a polynomial curve fit with 8 coefficients:

$$ln\lambda_i = c_1 ln\, T + \frac{c_2}{T} + \frac{c_3}{T^2} + c_4,\ T > 1000K \tag{2.13-a}$$

$$ln\lambda_i = c_5 ln\, T + \frac{c_6}{T} + \frac{c_7}{T^2} + c_8,\ T < 1000K. \tag{2.13-b}$$

The multi-species mixture conductivity is the result of combination averaging of single species thermal diffusivities:

$$\lambda_{mix} = \frac{1}{2}\left(\sum_{i=1}^{N} \lambda_i X_i + \left(\sum_{i=1}^{N} \frac{X_i}{\lambda_i}\right)^{-1}\right). \tag{2.14}$$

Finally, assuming unity Lewis number , the mixture mass diffusivity is computed from eq (2.15):

$$D_{mix} = \frac{\lambda_{mix}}{\rho c_p Le}. \quad (2.15)$$

2.5 Reaction Mechanism

We use a detailed 9 species, 19-step reaction mechanism attributed to[41] to describe $H_2$-$O_2$ reaction kinetics in FLASH. The forward reaction rates are given by the Arrhenius equation:

$$k_{fj} = AT^{-\alpha}\, e^{-\frac{E_g}{TR}}\ , \quad (2.16)$$

where $A$ is the pre-exponential factor, $\alpha$ is the temperature index and $E_g$ is the activation energy. To compute the backward reaction rates ($k_{bj}$), we first calculate the equilibrium constants ($K_c$) as a function of the species concentration, and corresponding changes in the Gibbs free energy ($\Delta G_T$) due to changes in temperature[42]:

$$K_c = \left(\frac{RT}{P}\right)^{-\Delta\upsilon} e^{\left(\frac{\Delta G_T}{RT}\right)} \quad (2.17)$$

In eq. (2.17), $\Delta\upsilon$ is the change in the mole number between reactants and products. The backward reaction rates are then obtained from:

$$k_{bj} = \frac{k_{fj}}{K_c}. \quad (2.18)$$

The resulting system of N number of ODEs (governing N species) is solved using an implicit Bader-Deuflhard [43] scheme in FLASH in conjunction with a MA28 linear algebra package [44]. Finally, the energy generated over each time step *dt* is computed using

$$e_g = \sum_1^N \frac{h_{f_i}}{A_j} (Y_t - Y_{i_{t+\Delta t}}), \quad (2.19)$$

where $h_{fi}$ is the heat of formation and $Y_{i,t}$ and $Y_{i,t+dt}$ are mass fractions of the $i^{th}$ species at times t and $t+dt$ respectively. For a detailed summary of modifications to FLASH and validation efforts, we refer the reader to [35].

2.6 Problem Setup

We study the interaction of a Mach 1.58 shock with an initially diffuse, multimode interface between Hydrogen and Oxygen in the numerical shock tube configuration shown in fig. 1(a). The concentration of hydrogen over the interface thickness varies as

$$Y_{H_2} = \frac{1}{2} erfc \left(\frac{\sqrt{\pi}(x - S(y,z))}{L/128}\right), \quad (2.20)$$

where $S(y,z)$ are the x-heights of perturbations on the interface at each $(y,z)$ coordinate and $L$ is the shock tube width. The shock originates in the light fluid ($H_2$) at x = $x_s$ and crosses the interface to the heavy fluid ($O_2$), depositing baroclinic vorticity at the contact line in the process. Due to the impedance mismatch between the gases, the shock-interface interaction results in a transmitted shock in $O_2$ (traveling at $W_t \approx 1.09\, e5$ cm/s), and a reflected shock in the light gas (with velocity $W_r \approx 0.77e5$ cm/s). For these conditions, the jump velocity ΔU acquired by the interface following the shock interaction is $\sim 7.1\, e4$ cm/s, in good agreement with predictions from the Rankine-Hugoniot conditions [45]. We impose a corresponding negative particle velocity (=-ΔU) throughout the computational domain, so that following the shock impact, the interface traverse is arrested. This allows us to extend our simulations to very late (self-similar)

times, without resorting to a large aspect ratio computational domain. The $O_2$ and $H_2$ streams are initialized at 300K and 1000 K respectively, so that the corresponding pre-shock Atwood number (At $\equiv\frac{\rho_{O_2}-\rho_{H_2}}{\rho_{O_2}+\rho_{H_2}}$) is 0.65. Density compression by the shock modifies the Atwood number to a post-shock value of 0.66 and is consistent with the estimate from Rankine-Hugoniot equations [45]. In our reacting RM simulations, density changes in the flame region due to ignition further modifies the maximum Atwood number to ~ 0.78 between Oxygen ($\rho_{O_2} = 1.06\, e-3\, g/c^3$) and flame ($\rho_{fl} = 1.36e-4\, g/c^3$) region.

The 3D numerical shock tube is shown in figure (1a) and has a square cross-section with dimensions 6 cm x 6 cm along the lateral (y-z) directions. In the direction of shock propagation (x-), the shock tube has a length of 9 cm (aspect ratio = 1.5) for all simulations reported here. Periodic boundary conditions were used along the lateral walls, while outflow conditions were implemented at the inlet and outlet surfaces to permit the reflected and transmitted shock waves to exit without acoustic reflections. We characterize the growth of the mixing layer by tracking the evolution of the mixture fraction (**Z**) defined as [46]:

$$\mathrm{Z} = \frac{\frac{0.5\,Z_H}{W_H}+(Z_{O,ox}-Z_O)/W_O}{\frac{0.5\,Z_{H,fu}}{W_H}+\frac{Z_{O,ox}}{W_O}}, \qquad \text{(2.21-a)}$$

where,

$$Z_O = W_O\left(2\frac{Y_{O_2}}{W_{O_2}}+\frac{Y_O}{W_O}+\frac{Y_{H_2O}}{W_{H_2O}}+\frac{Y_{OH}}{W_{OH}}+2\frac{Y_{HO_2}}{W_{HO_2}}+2\frac{Y_{H_2O_2}}{W_{H_2O_2}}\right) \qquad \text{(2.21-b)}$$

and

$$Z_H = W_H\left(2\frac{Y_{H_2}}{W_{H_2}} + \frac{Y_H}{W_H} + 2\frac{Y_{H_2O}}{W_{H_2O}} + \frac{Y_{OH}}{W_{OH}} + \frac{Y_{HO_2}}{W_{HO_2}} + 2\frac{Y_{H_2O_2}}{W_{H_2O_2}}\right). \quad (2.21\text{-c})$$

In this notation, $W_i$ and $Y_i$ are the molecular weights and mass fractions of species $i$, while $Z_{H,fu}$ and $Z_{O,ox}$ are the values of $Z_H$ and $Z_O$ within the pure fuel and oxidizer streams. In our study, $Z_H = Z_O = 1.0$, so that the fuel and oxidizer streams are free from dilution. In contrast with other scalar quantities that experience fluctuations and rapid gradient changes, the mixture fraction defined in eq. (2.21) satisfies monotonicity across the mixing zone for both reacting and non-reacting flows and thus provides a consistent basis to compare the two. As a result, we use the planar (y-z) average of the mixture fraction <Z> to compare the properties of the reacting and non-reacting RM flows and to diagnose the growth of the mixing layer in each case.

The initial material interface between the fuel and oxidizer is perturbed according to the multimode function prescribed by [47] where the perturbation amplitudes are specified according to:

$$h\left(y, z, t = 0\right) =$$

$$\sum_{k_y k_z}\{a_k\, cos\left(k_y y\right) cos(k_z z)) + b_k\, sin\left(k_y y\right) cos(k_z z)) +$$

$$c_k\, cos\left(k_y y\right) sin(k_z z)) + d_k\, sin\left(k_y y\right) sin(k_z z))\} \quad (2.22)$$

Note that $a_k$, $b_k$, $c_k$ and $d_k$ are modal amplitudes specified as random functions, but with energy concentrated in modes 8 – 16. Additionally, a random phase is added to each term to avoid concentrated peaks and valleys in the perturbation function. The rms amplitude of the perturbation was specified to be $\approx 0.1\lambda_{min} = 0.0375\, cm$, to ensure every mode in the initial conditions evolves first with a linear growth rate (i.e. $kh_0 << 1$).

Figure1 (b) shows the initial interface with the imposed perturbation field h(y,z) from eq. (2.22). The simulations were performed with Adaptive Mesh Refinement (AMR) with resolution equivalent to a uniform mesh of 256 (448) zones/L in all directions for the non-reacting (reacting) simulations. At this mesh resolution, the shortest waves in the initial condition wavepacket ($\lambda_{min}$) would be resolved with 32 zones spanning the wavelength. A detailed discussion and justification of the grid resources employed in our simulations is presented in the appendix.

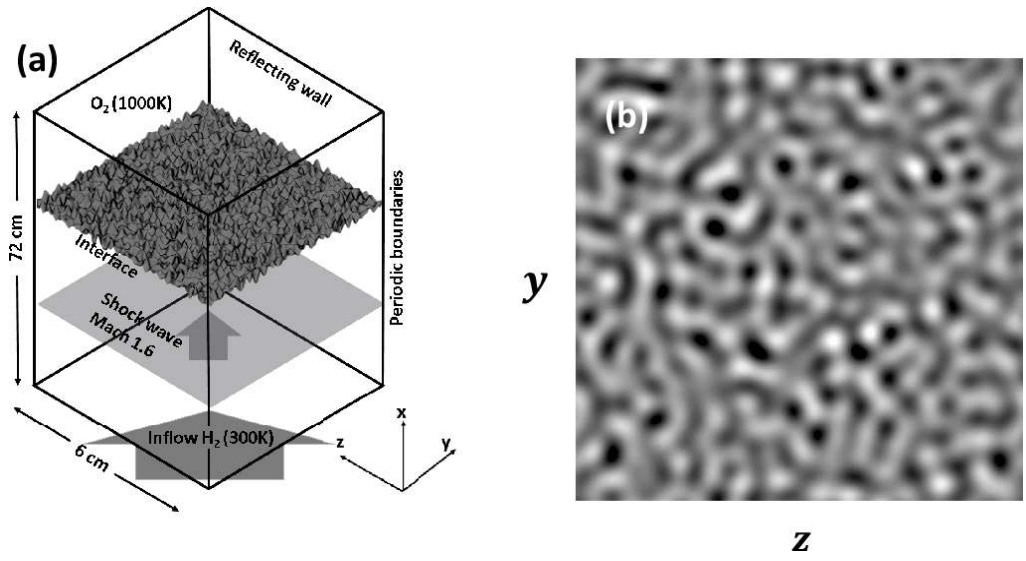


Figure 2.1: (a) Problem configuration employed in FLASH simulations of multi-mode reacting and non-reacting RM Instability and (b) initial mixture fraction perturbation field imposed on the interface.

# CHAPTER 3: SIMPLE CONFIGURATIONS OF SHOCK DRIVEN NON-PREMIXED COMBUSTION

In this chapter, we analyze simpler configurations of shock driven non-premixed combustion with the objective of providing some insight into the phenomena. The analysis in this chapter was performed on simulations that were carried out by [35,48- and reported therein. First, we describe shock-driven combustion of an $H_2$ bubble in air[35]. In the second problem we study the results of simulation [48] of the interaction of a shock wave with a sinusoidal interface between $H_2$ and $O_2$.

## 3.1 Shock-Bubble Interaction: Configuration

A spherical hydrogen bubble moves toward and interacts with a stationary planar shock wave of Mach number 2. The problem configuration is according to [49] and is shown schematically in figure 3.1. The physical domain for this 2D problem consists of a rectangular domain of dimensions 3cm by 1.5 cm. The $H_2$ bubble diameter is 0.5 cm while the stationary shock wave is located at x = 0.7. The hydrogen bubble approaches the shock with an ambient velocity Uu= 1.24e5 cm/s. The initial distance between the bubble surface and the shock is 0.2 mm, the pre-shock temperature and pressure specified to be 1000 K and 1 atm respectively, for both air and the hydrogen bubble. The shocked air on the left side of the domain is initialized with ambient velocity of US= 4.3e4 cm/s,

temperature of 1565 K and pressure of 4.4 atm. The mass fraction for $H_2$ bubble as a function of radius is specified by [41]:

$$Y_{H_2} = \frac{1}{2}\left[1 + tanh\left(\frac{r_c - r}{S}\right)\right] \quad (3.1)$$

$$r = \sqrt{(x - x_0)^2 + (y - y_0)^2} \quad (3.2)$$

where $S$ represents the sharpness of the interface, $r_c$ is the bubble radius and $(x_0, y_0)$ determine the location of the bubble center. As stated in [35], $S$ was chosen to be 3, which yields a value of 2.5e-2 cm for the initial interface thickness. As a result of the interaction between the shock wave and the bubble, shock waves travel towards the right outlet boundary at x=3 cm. Both inlet and outlet boundary conditions are set as outflow surfaces. Numerical mass diffusion and implicit thermal and viscous diffusion were used in this simulation [35]. The implicit diffusion solver was employed over a uniform grid with 1280x640 zones resolution. Viscosity and thermal conductivity were calculated using combination averaging formulas given in [50]. Combustion of hydrogen and oxygen has been modeled by detailed chemistry involving 9 species and 19 step reversible reaction mechanisms [41].

## 3.2 Shock-Bubble Interaction: Discussion

Figure (3.2) shows contours of Temperature, $H_2O$ mass fraction and magnitude of vorticity at different times. In fig. 3.2 (a), the shock has just hit the bubble and compressed the interface. Temperature increases at points of shock impact, while the mass fraction of $H_2O$ is insignificant at this stage, since there has been insufficient mixing and combustion up to this point in the simulation. Thus, temperature increases are confined to localized regions within the computational domain. At t = 10 μs, (fig. 3.2

(b)), a large portion of $H_2$ has traveled into the shocked region; the temperature has reached about 2000 K in the reaction zone (the narrow C-shaped region), where $H_2O$ is being produced as a result of combustion. The magnitude of $H_2O$ mass fraction and vorticity is still small compared to their values at late times. At t = 20 μs (fig. 3.2 (c)), there is significant vorticity accompanying high values of $H_2O$ mass and a large reaction zone, that is visible from the temperature contours. At t = 40 μs, large areas of mixing are visible, but the peaks of each quantity decrease. This occurs due to the limited amount of fuel ($H_2$), in the domain, the mass fraction of which is constantly decreasing so that by t = 40 μs, the fuel is completely used up. Fig. 3.3 shows the pressure field and $Y_{H2}$ at t = 3.5 μs. The pressure distribution on the dashed line is shown in Fig. 3.4. The figure shows the pressure distribution along y = 0 cm, from FLASH and the results presented in [41], and shows very good agreement between our simulations and those of [41]. In the figure, the transmitted shock wave can be seen as a local maximum value at x ~ 0.43 cm. The local peak at x ~ 0.55 cm is associated with the reflected shock, returning from the left side of the compressed bubble, while the local maximum at x ~ 0.7 cm shows the reflected shock wave coming from $H_2$-Air interface on the right side of the compressed bubble. In fig 3.5, we plot the time evolution of the integral heat release rate, total circulation within the domain, and the rate at which total mass of $H_2O$ inside the computational domain is changing. All quantities have been scaled to fit within the same plot. The total mass of $H_2O$ within the domain is calculated by

$$M_{H_2O} \equiv \int Y_{H_2O} \rho dV \tag{3.3}$$

where, $Y_{H2O}$ and $\rho$ are the mass fraction of $H_2O$ and density. Similarly the integral heat release rate is defined according to

$$C \equiv \int_0^{\infty} \frac{<e_g>}{\Delta t} dx \tag{3.4}$$

where, $e_g$ is the heat added per unit mass due to combustion over a simulation timestep $\Delta t$ , and <·> indicates planar averaging along the y - direction. Finally, the total circulation within the domain is defined using equation (3.5).

$$\Gamma = \iint_A \vec{\omega}.\vec{A} \tag{3.5}$$

Here, $\vec{\omega}$ is the vorticity vector and $\vec{A}$ is the area vector normal to the plane. The rate at which total mass of $H_2O$ inside the computational domain is changing is given by

$$\dot{M}_{H_2O} \equiv \frac{\Delta M_{H_2O}}{\Delta t}. \tag{3.6}$$

Fig. 3.5 shows the onset of circulation within the domain coincides with the arrival of the shock at t = 1.5 μs. This process is driven by the deposition of baroclinic vorticity by the incident shock. Following the initial increase the circulation is nearly constant for this flow. The integral heat release rate and the rate of formation of product ($\dot{M}_{H_2O}$) closely track the progress of combustion within the domain. Both quantities report an initial increase around t ≈ 6 μs, by which time the entire bubble has been engulfed by the shock. Peak values of the quantities are achieved at t ≈ 15 μs, following which C and $\dot{M}_{H_2O}$ decay owing to the depletion of available fuel in the domain. In contrast, the total mass of $H_2O$ in the domain increases monotonically in these simulations by [35], as expected.

From plotting the integral properties directly against each other, it is possible to draw conclusions on the extent of correlation between them. In fig. 3.6 we plot the integral heat release rate against the rate of formation of $H_2O$. Both quantities reflect the

progress of combustion in the flow and are in a sense, markers of that process, thereby exhibiting a strong correlation. In contrast, the correlation between the total circulation and integral heat release rate (fig. 3.7) or the rate of formation of $H_2O$ (fig. 3.8) appear weak. This follows from the trend in fig. 3.7, where the combustion lags the deposition of circulation within the flow. The onset of combustion in fig. 3.7 occurs after significant circulation has been deposited by the shock, resulting in mixing process that culminates in combustion.

### 3.3 Single-Mode Reacting RM: Configuration

Here the material interface is specified as a single-mode, sinusoidal function. When a shock wave passes through a perturbed interface between two fluids with different densities, the perturbations grow. The problem considered by [35], consists of a 2D shock tube with an aspect ratio of 6. The shock tube has outflow boundary conditions at x=0 cm and reflecting boundary conditions at x=36 cm. Periodic boundary conditions are applied at the lateral boundaries. Reflecting boundaries at x=36 cm will cause a reflecting shock which hits the burning interface resulting in increase in mixing and combustion efficiency. Hydrogen is the light fluid (at 300 K), and is separated from air (at 1650K) by a diffuse interface. Initial values for density of hydrogen and oxygen are 8.0e-5 g/cm3 and 2.4e-4 g/cm3, resulting in an Atwood number of 0.5. The incident shock has a Mach number of 1.2 and a pressure ratio of 1.51. The shock is initially located immediately next to the interface in the hydrogen gas and travels toward the interface, where the initial interface location is defined by:

$$x_i = +\frac{\Delta}{2} + h_0\left[1 - cos\left(\frac{2\pi y}{\lambda}\right)\right] \tag{3.7}$$

where $x_s$ is the initial location of the shock, h0 is the initial amplitude and λ is the wavelength. In our simulation λ = 6 cm, and $h_0$ = 0.2/k, where k is the wavenumber (k = 2π/λ). The mixture fraction is calculated according to the following formulation:

$$Z = \frac{8Y_{H_2} - Y_{O_2} + 1}{9} \tag{3.8}$$

where, $Y_{H_2}$ and $Y_{O_2}$ are the hydrogen and oxygen mass fractions. The mixture fraction is assumed to vary as an error function defined over a thickness equal to two times the amplitude,

$$Z(x) = \frac{1}{2}\left\{1 - erf\left[(x - x_i)\frac{W}{4}\right]\right\} \tag{3.9}$$

where, $W$ is a scaling factor defined by:

$$W = 2[erf^{-1}(1 - \varepsilon)] \tag{3.10}$$

This definition of mixture fraction ensures a continuous function and is a reliable parameter to compare reacting and non-reacting RMI. While mass fraction can become discontinuous across the interface, the mixture fraction changes in a monotonic manner. A schematic of the problem setup is shown in figure 3.9.

### 3.4 Single-Mode Reacting RM: Discussion

Figure 3.10 exhibits the time evolution of temperature, $H_2O$ mass fraction and magnitude of vorticity contours for the reacting single mode Richtmyer Meshkov Instability. Contours are plotted at t = (a) 3.5 ms, (b) 0.6 ms, (c) 1 ms and (d) 2.1 ms. Reshock occurs at t = 0.6 ms, when the interface is already in the nonlinear regime. Following reshock, phase inversion can be seen between images (b) and (c). As depicted in fig. 3.11, all three integral flow quantities of interest follow same trend. The highest

temperature occurs in the region of the highest $H_2O$ mass fraction where the magnitude of vorticity is the largest as well.

The time evolution of $M_{H_2O}$, $\dot{M}_{H_2O}$, C and $\Gamma$ are shown in fig. 3.11 for the data from single-mode reacting RM simulation of [35]. Following the initial shock, these quantities exhibit gradual growth until t≈0.6ms, when reshock occurs. Following the interaction of the reflected shock with the already nonlinear interface, the mixing and combustion is significantly enhanced within the domain. The lag between the total circulation deposition and the quantities associated with combustion is reduced in this case (compared to fig. 3.5), since the circulation deposition along the entire interface occurs instantaneously, thus immediately triggering combustion and heat release all along the interface.

A plot of integral $H_2O$ production rate versus the integral heat release rate displays nearly-perfect correlation as anticipated. Due to the localized deposition of circulation, the entire interface ignites at the same time, and immediately upon shock passage. This ignition, results in improved correlation between each of the combustion quantities (C and $\dot{M}_{H_2O}$ in fig. 3.13 and 3.14 respectively) and total circulation in the domain. In each plot, the inset shows data points associated with the first shock.

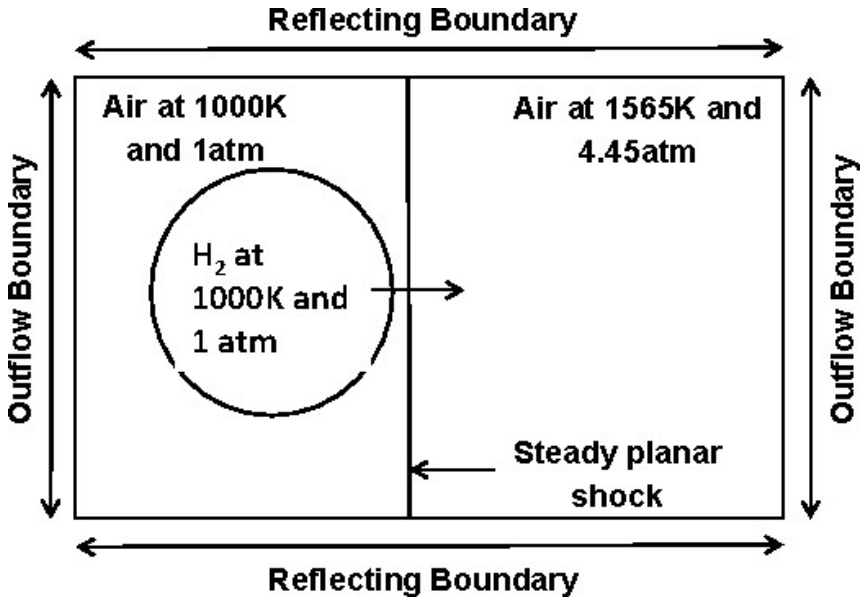


Figure 3.1: Schematic of the problem setup for the reacting shock-bubble simulation.

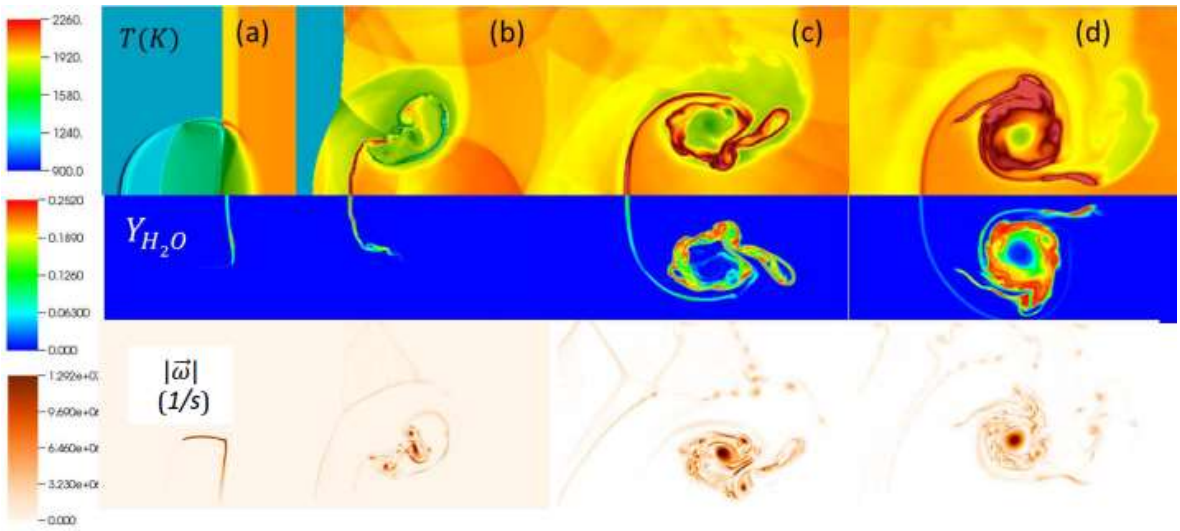


Figure 3.2: Time evolution of Temperature, $H_2O$ mass fraction and magnitude of vorticity from 2D simulations of a shock-bubble flame. Images are realized at t = (a) 1.5 μs, (b) 10 μs, (c) 20 μs and (d) 40 μs.

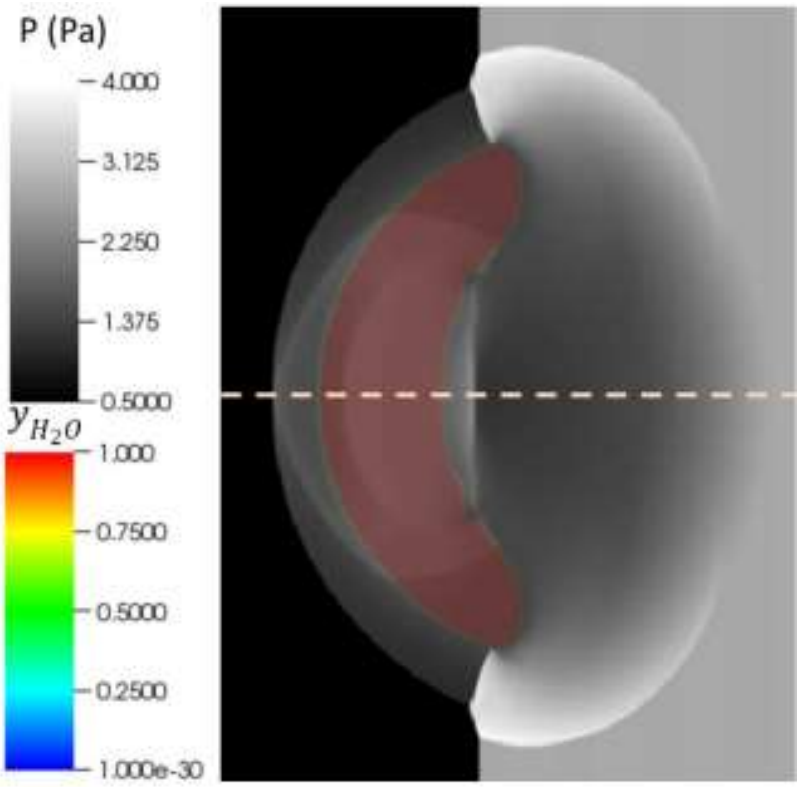


Figure 3.3: Contours of Pressure and $\boldsymbol{Y_{H2O}}$ at t = 3.5 μs after shock incidence

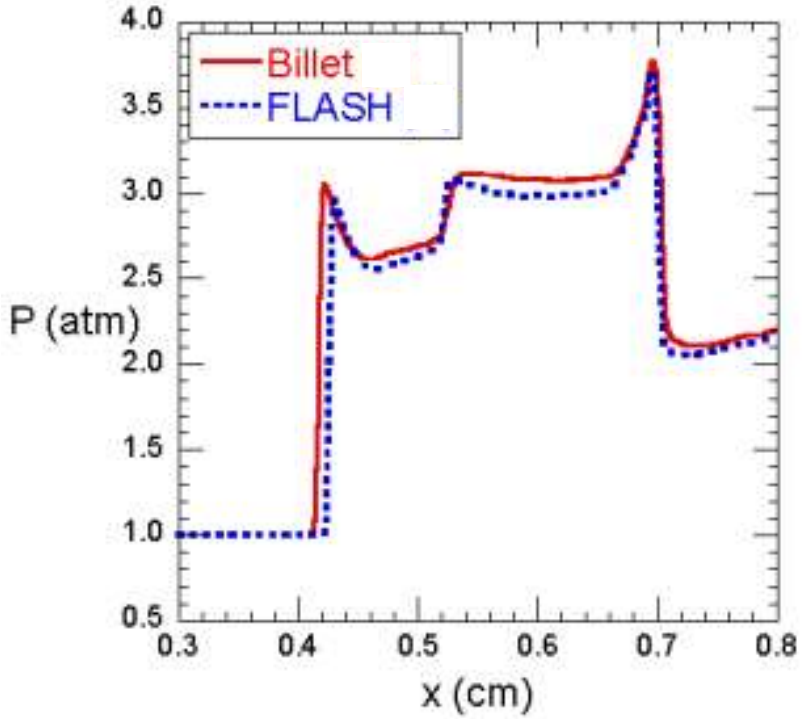


Figure 3.4: Pressure across y =0.0 cm, at t = 3.5 μs in the shock bubble interaction from FLASH and Billet [41]

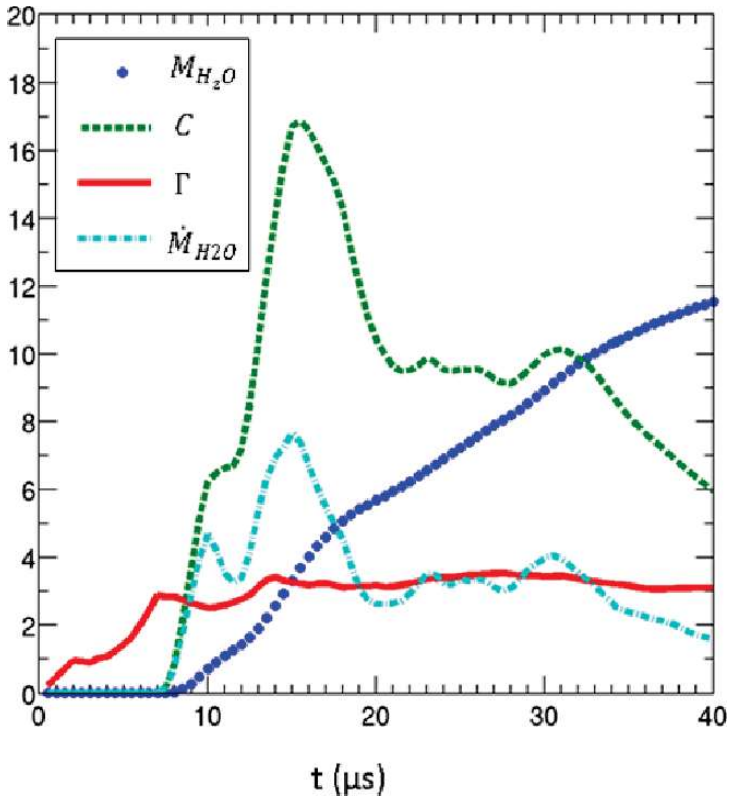


Figure 3.5: Total mass of $H_2O$ ($\boldsymbol{M_{H2O}}$, 1e-4 g), Integral heat release rate($\boldsymbol{C}$, 1e13 erg/s), total circulation inside the domain ($\boldsymbol{\Gamma}$, 1e5 $cm^2/s$), and Integral H2O addition rate ($\dot{M}_{H_2O}$, 1e-1 g/s) versus t (ms)

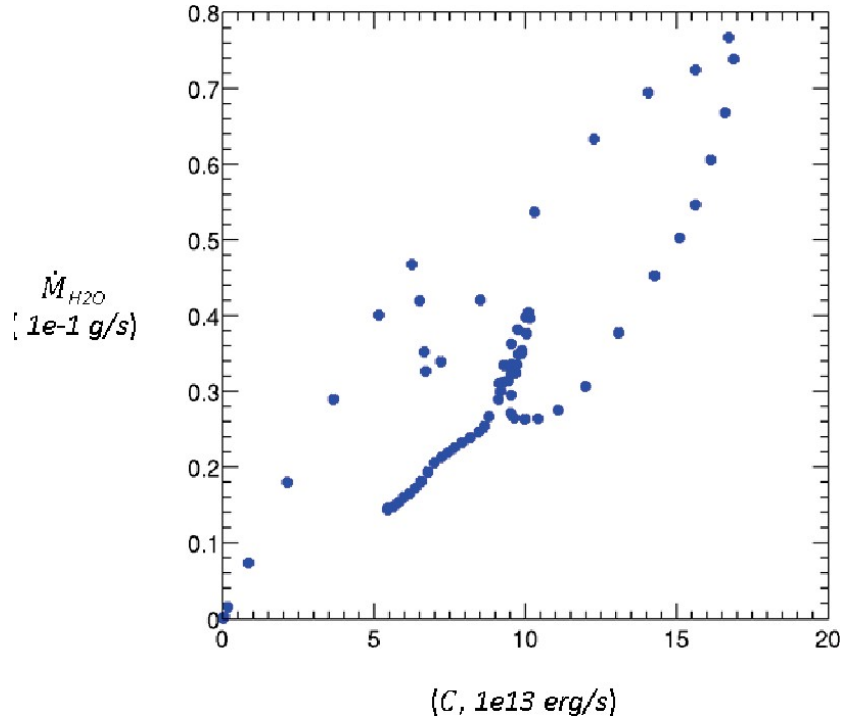


Figure 3.6: Integral $H_2O$ addition rate ($\dot{M}_{H_2O}$, 1e-1g/s) versus Integral heat release rate ($\boldsymbol{C}$, 1e13 erg/s)

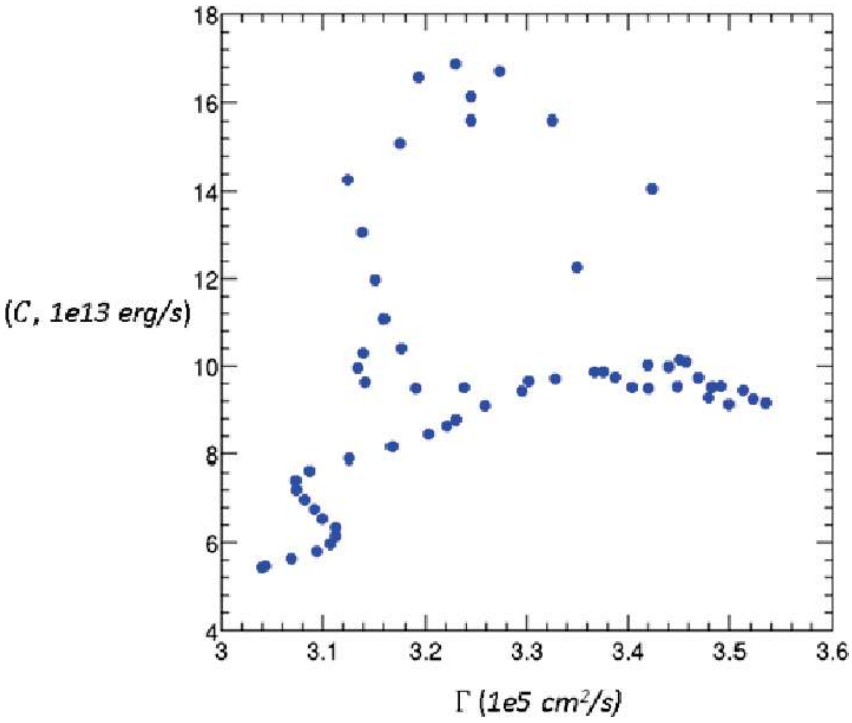


Figure 3.7: Integral heat release rate ($\boldsymbol{C}$, 1e13 erg/s) versus total circulation inside the domain ($\boldsymbol{\Gamma}$, 1e5 $cm^2/s$)

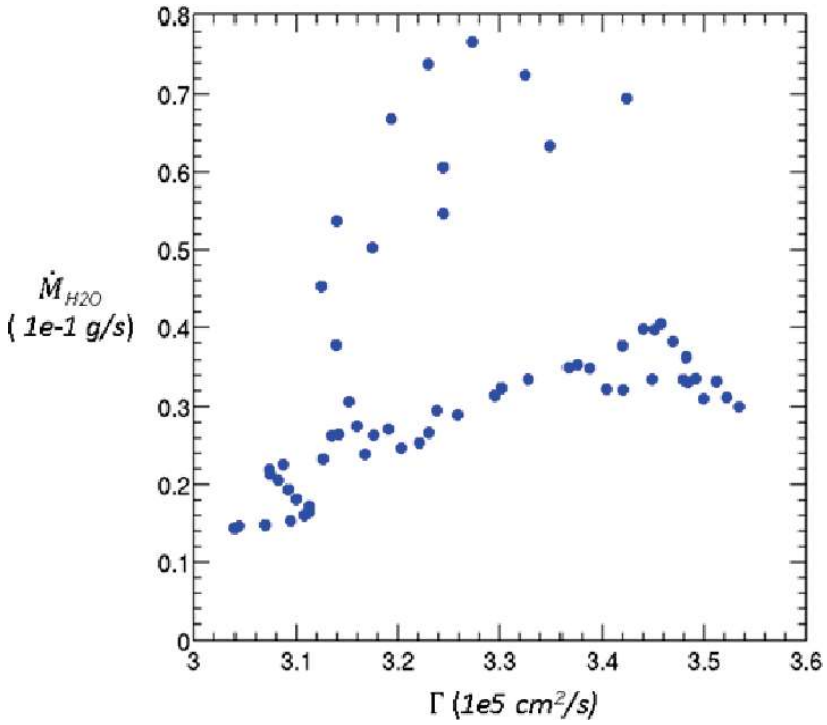


Figure 3.8: Integral $H_2O$ production rate ($\dot{M}_{H_2O}$, 1e-1 g/s) versus total circulation inside the domain ($\boldsymbol{\Gamma}$, 1e5 $cm^2/s$)

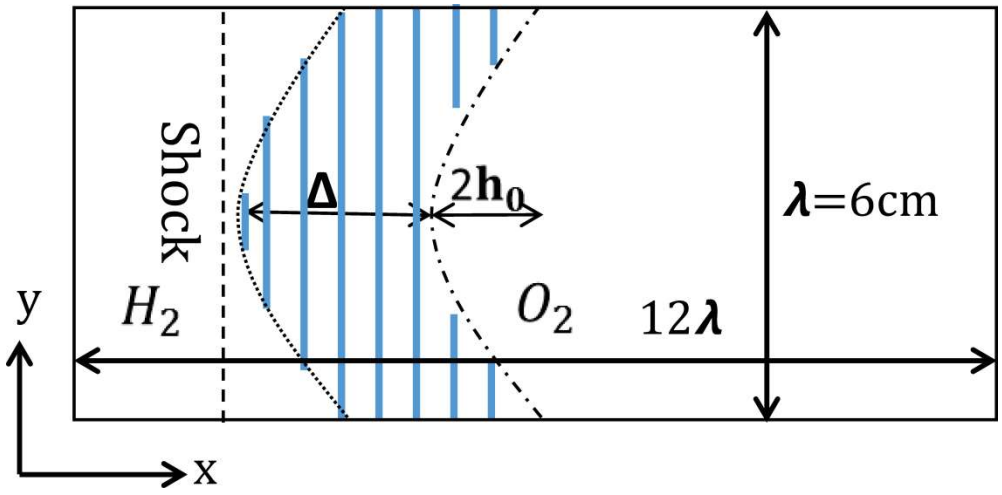


Figure 3.9: Schematic of the problem setup for Single mode RMI Simulation.

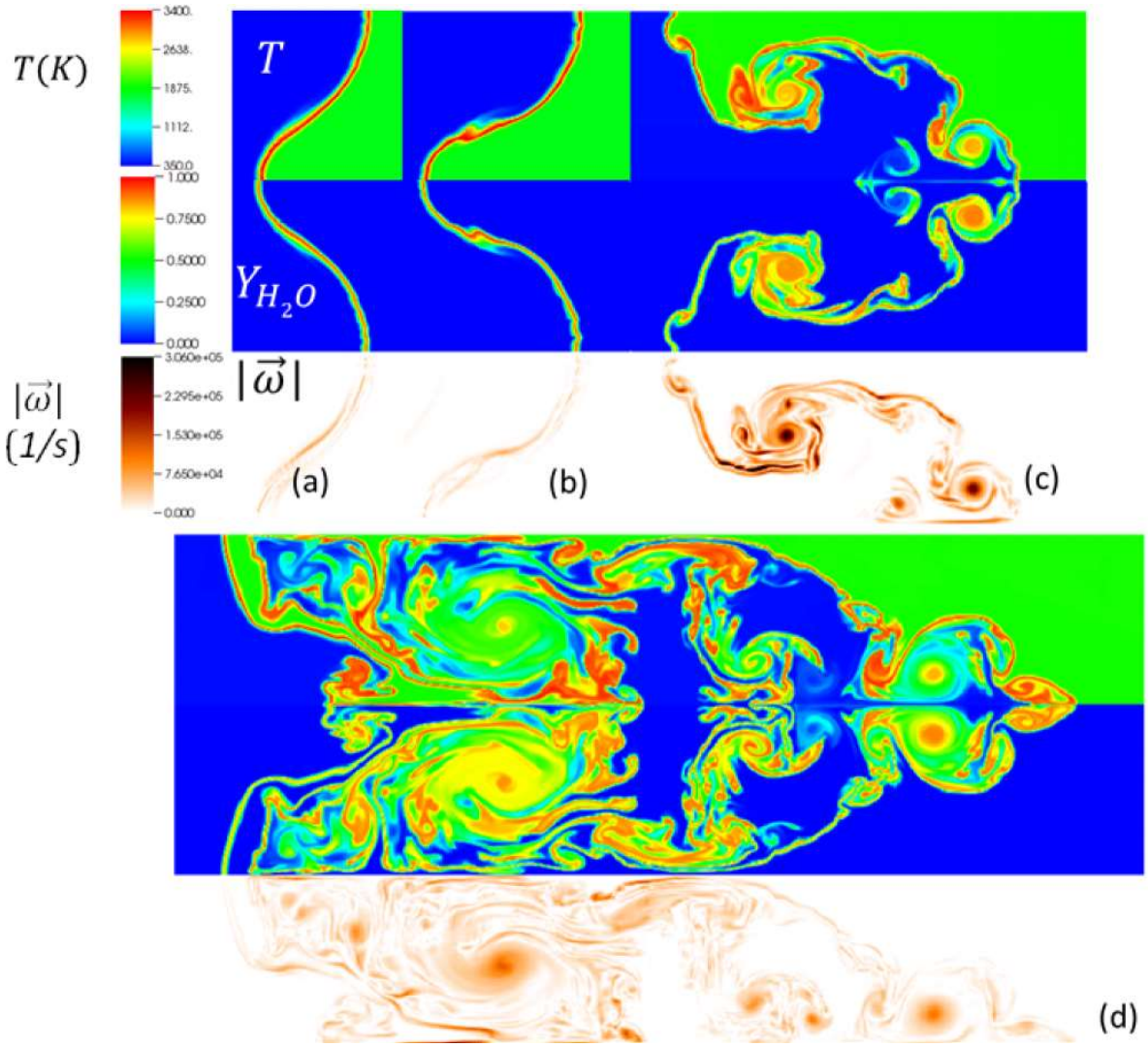


Figure 3.10: Time evolution of Temperature, H2O mass fraction and magnitude of vorticity from 2D simulation of a single mode perturbed, reacting interface. At t = (a) 0.35 ms, (b) 0.6 ms, (c) 1 ms and (d) 2.1 ms

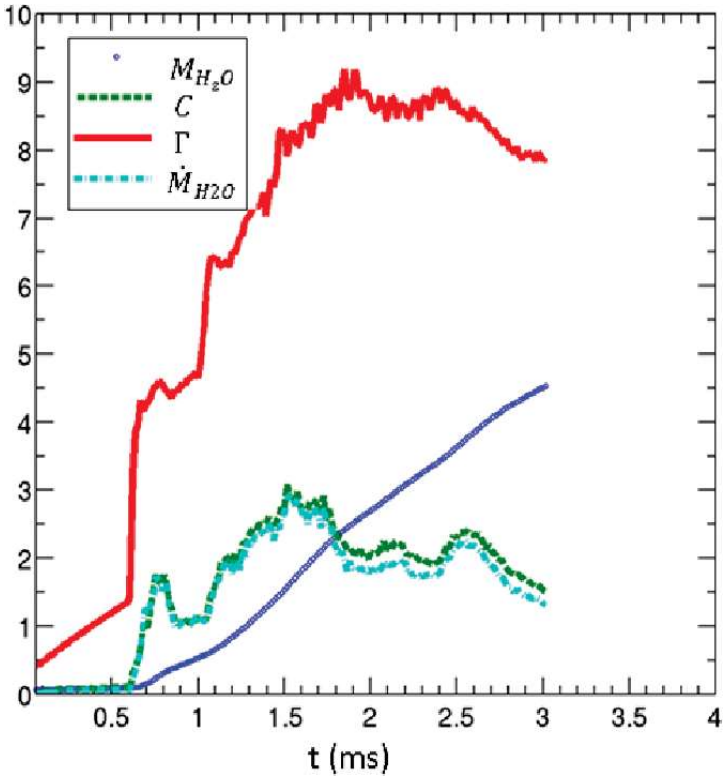


Figure 3.11: Total mass of $H_2O$ ($\boldsymbol{M_{H2O}}$, 1e-3 g), Integral heat release rate ($\boldsymbol{C}$, 1e15 erg/s), total circulation inside the domain ($\boldsymbol{\Gamma}$, 1e5 cm2/s) and, Integral $H_2O$ addition rate ($\dot{M}_{H_2O}$, g/s) versus t (ms)

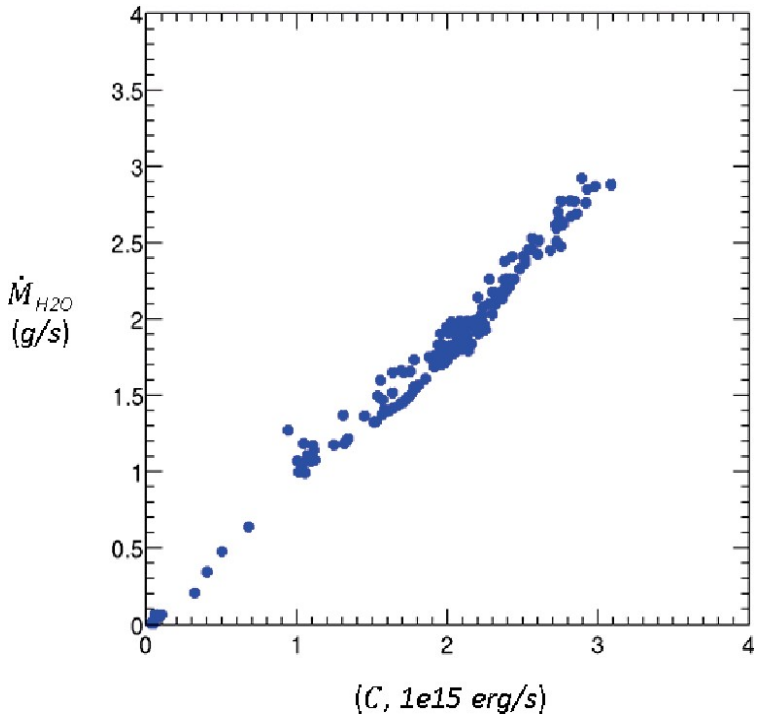


Figure 3.12: Integral $H_2O$ production rate ($\dot{M}_{H_2O}$, g/s) versus Integral heat release rate ($\boldsymbol{C}$, 1e15 erg/s)

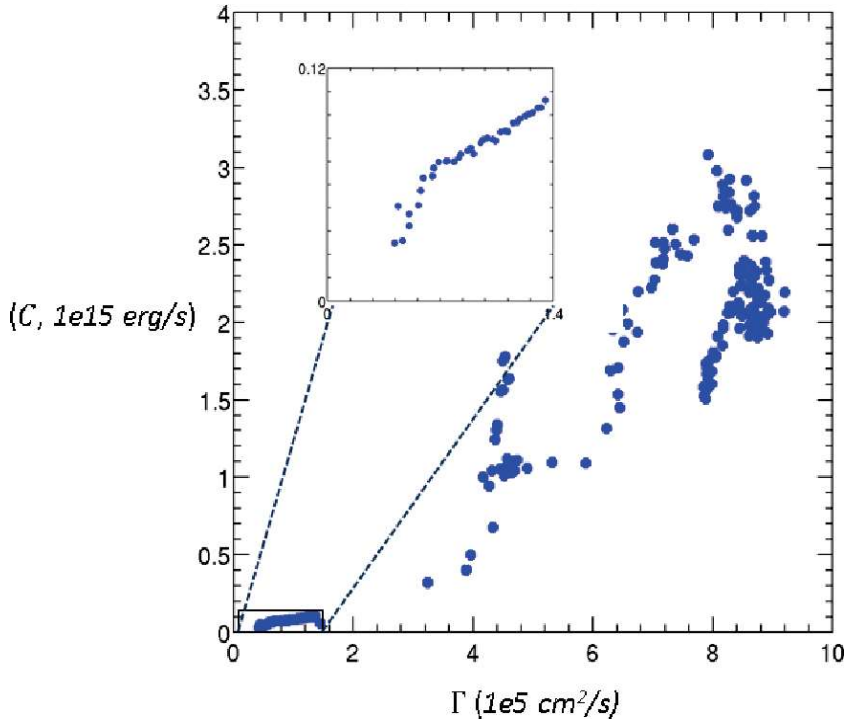


Figure 3.13: Integral heat release rate ($C$, 1e15 erg/s) versus total magnitude of vorticity within the domain ($\Gamma$, 1e5 cm2/s)

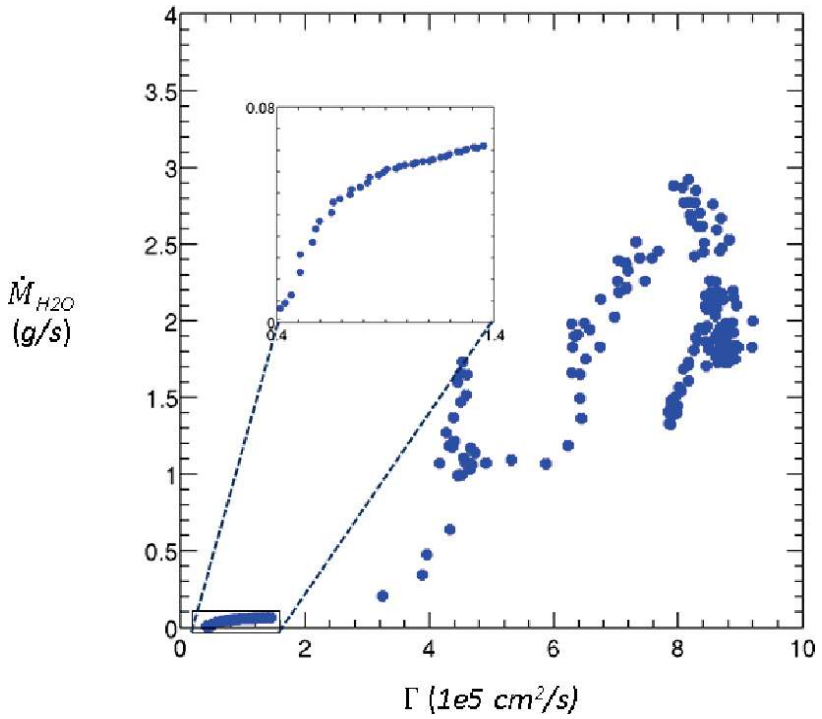


Figure 3.14: Integral $H_2O$ addition rate ($\dot{M}_{H_2O}$, g/s) versus total magnitude of vorticity within the domain ($\Gamma$, 1e5 $cm^2/s$)

# CHAPTER 4: REACTING AND NON-REACTING TURBULENT FLOW PROPERTIES

In this chapter, we study the effect of combustion heat release in forming hydrodynamic instabilities in the flow by analyzing the unperturbed interface behavior. Then, we discuss methods to compute the Reynolds number in RM driven flows and apply them to our problem.

## 4.1 Unperturbed (1D) Interface Dynamics

Before describing the complex, spatiotemporal behavior of the turbulent reacting RM, we briefly discuss the shock and interface dynamics of the 1D unperturbed reacting flow in this section. The 1D flow configuration is similar to the problem setup outlined in § 2.6, but with ($a_k$,$b_k$,$c_k$,$d_k$) = 0.0 in eq. (2.22) so that the mixture fraction interface is unperturbed. In figures 4.1 (a) and (b), we plot cross-stream (x-) profiles of scaled density ($\rho^* = \frac{\rho-\rho_l}{\rho_h-\rho_l}$), temperature ($T^* = \frac{T-T_l}{T_h-T_l}$) and pressure ($p^* = \frac{p-p_l}{p_h-p_l}$) at different dimensional times of interest (the dimensionless time $\tau$, is defined as $\tau \equiv tA^+\Delta U/\lambda_{min}$ [32]). Immediately following ignition, figure 4.1 (a) shows the presence of the incipient flame in the form of modest increases in the local temperature and pressure at $\tau = 1.3$. The transmitted shock and rarefaction fan are also visible in the cross-stream pressure profiles at these early times, fig. 4.1 (a). Figure 4.1 (b) is realized at $\tau = 2.5$, and shows

the reaction zone following ignition is marked by a substantial region with $\rho^* < 0$. Thus, the reacting RM experiences a net increase in the effective Atwood number near the flame surface – the presence of the intervening reaction zone results in an effective Atwood number of ~ -0.78 between pure $O_2$ and the combustion products, while the interface between the combustion products and pure $H_2$ is characterized by A ~ 0.29. By $\tau \approx 2.5$, significant burning has occurred (enabled by diffusion) and is accompanied by substantial local heat release and temperature rise. The reaction zone is highlighted by the presence of an active third layer of gases (products) with a density of 0.75e-3 g/cm$^3$ and temperature of 3050 K. The maximum temperature of 3050 K obtained in the flame region ($x|_{Z=0.11}$) is in good agreement with the adiabatic flame temperature of 3173 K for $H_2$-$O_2$ flames [51,52]. The sudden temperature increase resulting from ignition gives rise to a weak pressure wave seen in figure 4.1 (b). The pressure peak associated with this combustion wave is ~1.83e6 dyn/cm$^2$, and generates a local pressure jump $\frac{p_{combustion}}{p_{sho\quad region}} \sim 1.12$ that splinters in to two daughter waves. These waves travel with sonic velocity away from the flame and towards the fuel and oxidizer streams respectively. Thus, in addition to the shock-driven RM growth, the reacting mixing layer is also processed by short-lived pressure waves that impose a phase of variable acceleration RT instability [53,54] on the growth of the mixing layer (§5.1). We find the interface acceleration associated with the passage of the combustion waves in our simulations satisfies $g(t) \propto t^a$, with $a = -1.31$. Kuranz et al. [55] report a= -1.2 for a blast wave driven interface acceleration in a 2D experiment on the OMEGA laser. In 2015 Attal, et al. [48] calculated a = -1.8, where the blast wave was generated through combustion wave at an interface separating oxygen and hydrogen.

## 4.2 Reynolds Number of RMI Flows

In RM turbulence, the Reynolds number (Re) is of particular importance since it indicates the presence of turbulent flow [56]. In numerical simulations, knowledge of the expected Reynolds number may be used in determining the required grid resolution to resolve the corresponding Kolmogorov scales (Appendix A). From [13], an outer scale Reynolds number > 10000, implies turbulence levels beyond the mixing transition. For RMI (and RTI) the outerscale Reynolds number may be defined as:

$$Re = \frac{W\dot{W}}{\nu}, \tag{4.1}$$

where $W$ is the mixing width thickness, $\dot{W}$ is the mixing width growth rate and $\nu$ is the kinematic viscosity of the mixture. Recently, Weber at al. found Re calculated using eq. (4.1) associated with Mach numbers 1.6 and 2.2 to exceed 10e4 [56]. Similarly, Olson et al. [57] calculated Re in terms of the pre-shocked conditions and velocities of the gases, and found the Reynolds number to vary in the range 30000 - 180000 in the light and heavy gases respectively [57].

In RM flows, the Reynolds number may also be estimated based on the initial circulation deposited on the mixing layer due to shock passage [58]. According to this definition,

$$Re_\Gamma = \frac{\Gamma}{\nu}, \tag{4.2}$$

where Γ is the circulation of the vortex core and is defined by $\Gamma = \int_a \omega \, da$ , where $\omega$ is the baroclinic vorticity and $a$ is the bounding area. For a sinusoidal perturbation, an estimate is provided in [59] for the initial circulation following shock incidence according to [59]:

$$\Gamma_0 = u_t \, (W_r + W_t)t - u_2 \, (W_i + W_t)t \, , \tag{4.3}$$

where $u_t$ is the particle velocity behind the transmitted shock, $W_r$ is the reflected shock velocity, $W_t$ is the transmitted shock velocity, $u_2$ is the particle velocity behind the incident shock, $W_i$ is the incident shock velocity, and $t$ is the shock passage time

$$t = \frac{2\eta_0}{W_i}, \tag{4.4}$$

where $\eta_0$ is the initial perturbation amplitude.

Tomkins et al. [60] compared Re from equations (4.2-4.4) and (4.1) and found agreement between these definitions within a factor of two. In this study, we evaluated Re according to eq. (4.1). Figure 4.2 shows the time evolution of Reynolds number in both reacting and non-reacting cases. As seen in figure 4.2, the Reynolds number reaches a maximum initial value of $\sim 18000$ in the non-reacting and $\sim 23000$ in the reacting case, above the threshold for turbulence [13,61]. Upon ignition, the mixing width in the reacting case experiences an expansion growth due to combustion-initiated RT instability (section 3.1). Thus, at early times, the reacting flow Reynolds number is higher than the corresponding non-reacting result. Additionally, as the flame evolves, the temperature increase resulting in an increase in the diffusive transport properties. For example, the kinematic viscosity sees an increase from ~0.76 St at ~500 K ($\tau \sim 0$) to ~2.6 St at ~3100 K ($\tau > 30$) accompanied by a decrease in the Reynold number for the reacting case.

Asymptotically, the Reynolds number trendline is consistent with the power law behavior associated with the mixing width. Substituting $W = A(t - t_0)^{\theta}$ (please see section 5.4 eq 5.3) into eq (4.1):

$$Re = \frac{A^2\theta(t-t_0)^{2\theta-1}}{\nu}. \tag{4.5}$$

From fig (4.2), Reynolds number from simulations is consistent with the power law decay calculated using eq (4.5). Hence eq (4.5) can be used for *a priori* calculations of Re number and other turbulent flow metrics such as Kolmogorov length scale.

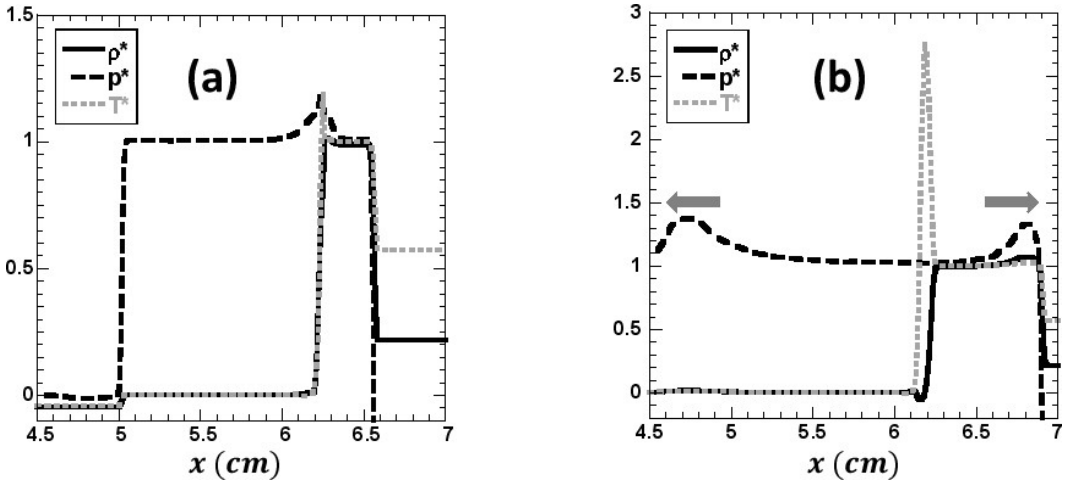


Figure 4.1: Cross-stream profiles of scaled temperature ($T^* = \frac{T-T_l}{T_h-T_l}$), scaled pressure ($p^* = \frac{p-p_u}{p_s-p_u}$) and, scaled density ($\rho^* = \frac{\rho-\rho_l}{\rho_h-\rho_l}$) at (a) $\tau$ = 1.3 and (b) $\tau$ = 2.5.

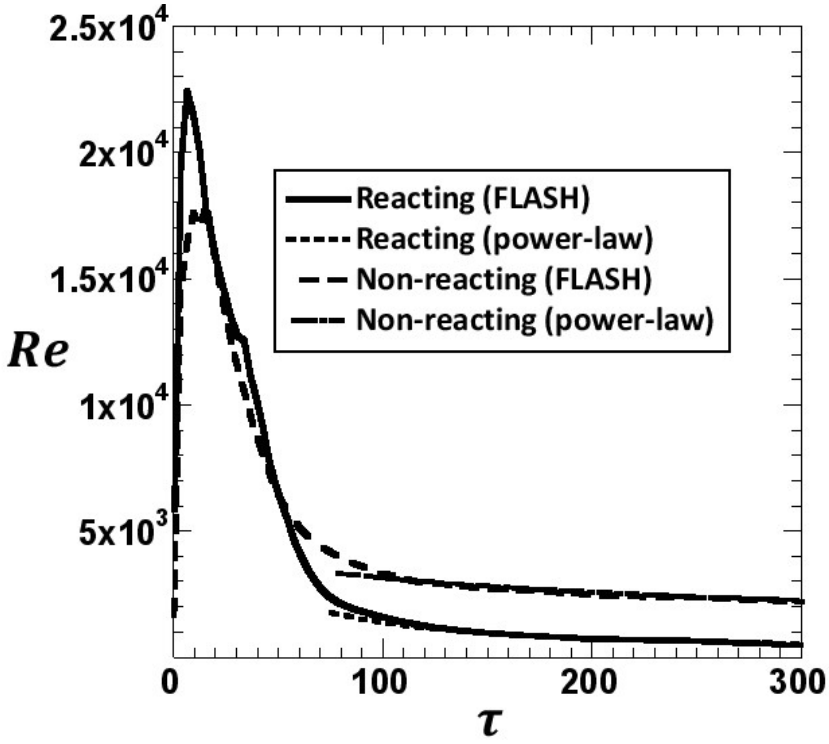


Figure 4.2: Reacting and non-reacting flow Reynolds number as a function of time from FLASH and power-law equation.

# CHAPTER 5: REACTING AND NON-REACTING TURBULENT MIXING FEATURES

In this chapter, we present a detailed discussion on evolution of mixing zone after the shock impact and following ignition . We also investigate the nature of self-similarity in reacting case and compare with corresponding non-reacting counterpart.

## 5.1 Evolution of Turbulent Mixing

When the interface is perturbed with a multimode function (eq. 2.22), the shocked mixing layer eventually achieves a turbulent state through nonlinear interactions involving saturated modes. The growth and interaction of modes can drive mixing and create conditions for sustaining combustion through the attendant turbulent diffusion process. In figures 5.1 (a) – (c), we show contours of the stoichiometric surface (Z = 11%) at early and late times from the reacting and non-reacting simulations. Following shock impact, the perturbations evolve through linear (fig. 5.1-a), nonlinear (fig. 5.1-b) and turbulent (fig. 5.1-c) stages. The slices are obtained at the mid-plane (z = 3 cm), and the solid white line in each frame indicates the location of the corresponding unperturbed interface (obtained from a separate simulation with $W_0 = 0$).

At early time ($\tau \approx 2.5$; fig. 5.1 a), the reacting RM mixing layer features slightly larger structures on the bubble and spike fronts compared to the corresponding inert

mixing layer. The observed development of bubbles and spikes at larger scales is due to the additional growth experienced by the reacting interface due to the passage of combustion waves, which result in a phase of variable-g RT instability. During this phase of RT growth, dominant bubbles (and spikes) that have matured through nonlinear growth evolve with $\langle\lambda_{b/s}\rangle \sim \langle h_{b/s}\rangle$, so that longer wavelengths are visible on the reacting front in fig. 5.1 (b). Note that the effect of combustion is more dominant on the bubble surface owing to its proximity to the flame sheet ($\langle Z\rangle = 0.11$), so that the reacting bubble amplitude growth outpaces its inert counterpart. In contrast, spike amplitudes (figure 5.1 (c)) from the reacting RM are in good agreement with the corresponding non-reacting flow at both early and late times. This is attributable to the large separation distance between the flame sheet and the spike surface ($\langle Z\rangle = 0.99$), so that combustion waves generated at the reaction zone have attenuated significantly before crossing the spike front.

Larger mixing width in the reacting case can be observed by looking at iso-surfaces of constant mixture fraction, figure 5.2 (a)-(c). At the initial stages of turbulent mixing in reacting flow, thermal expansion of hot combustion products generates an RT instability in the mixing zone and drives bubble and spike iso-surfaces in opposite directions. These phenomena can be seen as a sudden growth in the reacting mixing width compared to the non-reacting case, figure 5.2 (b). At late-times, the effect of RT instability in the reacting case has faded and Kelvin-Helmotz instabilities initiated by the RM instability drive mixing in both cases. At this stage, in the reacting case, enhanced diffusive interpenetration of $H_2$, $O_2$ and combustion products contributes in mixing

behavior in the reactive flow, which results in larger structures and less interrupted iso-surfaces in the mixing zone, fig 5.2 (c).

5.2 Self-Similarity

To elucidate the approach to self-similarity, we plot in figure 5.3, cross-stream profiles of the planar-averaged mixture fraction <Z> realized at different times against the scaled coordinate $\boldsymbol{\xi}$ :

$$\boldsymbol{\xi} \equiv \frac{\boldsymbol{x} - \boldsymbol{x}|_{<z>=50\%}}{\boldsymbol{x}|_{<z>=99\%} - \boldsymbol{x}|_{<z>=1\%}}. \tag{5.1}$$

This approach collapses cross-stream Z-profiles from both reacting and non-reacting simulations, while anchoring the profiles at $\xi = 0$ serves to highlight any underlying asymmetry between bubbles and spikes at these large Atwood numbers. Figure 5.3 (a) compares <Z> profiles of reacting and non-reacting cases at early times ($\tau \approx 30$) and shows the effects of ignition. The non-reacting <Z> profile reflects the asymmetry expected at $A^+ = 0.66$, through the appearance of greater spike penetrations observed at $\xi \rightarrow -0.5$. For the corresponding reacting profiles, the expansion of the interface due to its interaction with the combustion wave is evident in figure 5.3 (a) through longer tails associated with the bubble front. Scaled Z-profiles from both reacting and non-reacting simulations are plotted at late times ($\tau > 120$) in figures 5.3 (b) and (c) respectively. At these late times (figs. 5.3 (b) – (c)), the mixing layer appears to revert to self-similarity in both cases (evidenced by the collapse of Z-profiles) as the combustion-generated pressure waves recede from the interface. Note that in spite of the appearance of localized regions of $\rho^* < 0$ within the reaction zone, the mixture fraction profiles maintain their monotonicity, while preserving the same functional form as the non-reacting flow. This justifies our choice of Z as a consistent variable to track the growth of

the extent of the mixing zone in both the reacting and non-reacting cases, thus enabling a direct comparison between the two. However, cross-stream profiles from the reacting RM simulation show slight asymmetry towards $\xi \rightarrow 0.5$, with the appearance of a step-like feature due to bubble-side stretching. This stretching appears significant near the stoichiometric location ($Z_{st}$ = 11%) due to the presence of the reaction zone. As a result, the high level of diffusivity in the vicinity of the flame sheet results in a nearly uniform distribution of H atoms, leading to a region in which Z is nearly constant. This trend is consistent with the observation of longer bubbles in the sliced images of Z described above in the context of figure 5.1 (b)-(c).

5.3 Mixing Width

The growth of the mixing layer can be characterized quantitatively by tracking in time the integral mixing width, given by [32,65]

$$W(t) \equiv 6 \int < Z > (1 - < Z >)\, dx. \qquad (5.2)$$

Historically, W has been defined in terms of either the volume-fraction or mass fraction functions, but through the above discussion we have demonstrated the superiority of the mixture fraction as a diagnostic when directly comparing reacting and non-reacting flows. In figure 5.4 (a), we plot the evolution of the scaled integral mixing width ($W/W_0$) for both the reacting and non-reacting RM mixing layers against the scaled time $\tau$; where $W_0$ is the initial value of mix width before shock impact. Upon shock impact ($\tau$ = 0.6), the non-reacting mixing width evolves dominated by classical RM dynamics [3], and appears to satisfy $W \sim \tau^{\theta}$ consistent with earlier studies [31,32].

Following ignition, the mixing width associated with the reacting RM undergoes a sudden and significant expansion at $\tau \approx 1.5$ due to the acceleration produced by the

combustion pressure waves. From single-mode simulations, Attal and Ramaprabhu demonstrated the combustion waves in such flows bear some similarity to Taylor wave solutions [48], but with peak pressure values dependent on the initial diffusion layer thickness between the fuel/oxidizer streams. Since in the current simulations, the initial interface diffusion thickness is negligible compared to the shortest wavelength ($\delta/\lambda_{min} = 0.125$), the pressure waves generated from combustion are correspondingly weak and subsonic (Mach number $\approx 0.23$). By $\tau \approx 6$, these waves have exited the computational domain, so that eventually ($\tau > 40$) the effects of the combustion waves appear to be no longer important, and the mixing width resumes a power law dependence on time, consistent with an impulsively accelerated, but eventually decaying RM flow.

5.4 Power-Law Analysis of Mixing Width Growth Rate

As individual modes in the multimode wave packet attain nonlinear saturation, we analyze the reacting and non-reacting RM in terms of a self-similar mixing layer whose amplitude satisfies the power law behavior [28,32]:

$$W = A(t - t_0)^{\theta} \tag{5.3}$$

Thus, we characterize the growth rate of the integral mixing width in terms of the power law exponent θ, and compare our results with data from extensive studies of inert RM turbulence in the literature [32,66,67]. Following [32], we fit simulation data from both the reacting and non-reacting flows to the form suggested by eq. (5.3), while the parameters $A$, $t_0$ and $\theta$ may be obtained either through a nonlinear regression analysis or by directly evaluating the following derivative forms suggested by[32,68]:

$$\theta = \left(1 - \frac{W\ddot{W}}{\dot{W}^2}\right)^{-1}, \tag{5.4-a}$$

$$t_0 = t - \frac{(\theta - 1)}{\ddot{W}}\dot{W}, \tag{5.4-b}$$

$$A = \dot{W}\frac{(t-t_0)^{1-\theta}}{\theta}. \quad (5.4\text{-c})$$

Note that Clark and Zhou [67] propose an alternate representation for the power-law form of the mix width given by

$$W = W_{0c}\left(\frac{t+t_{0c}}{|t_{0c}|}\right)^{\theta}, \quad (5.5)$$

where $(W_{0c})$ is the mix width at $t_{0c}$, the virtual origin in time. In [67], the exponent $\theta$ was obtained by regressing W to simulation data over the range of $\frac{2}{7} < \theta < \frac{2}{5}$. Eq. (5.5) is algebraically identical to eq (5.3) and the computation of $\theta$ using these method yielded similar results, so $\theta$ from eq (5.5) is not included in table 1. We also evaluate the power law exponent θ using a third approach, by fitting FLASH simulation data to the RM growth model from [31]:

$$W = W_0^+\left(\frac{(X/X_0)-1}{\theta}+1\right)^{\theta}. \quad (5.6)$$

In equation (5.6), $W_0$ is the initial perturbation amplitude that seeds the RM growth, and may be itself be the end result of an RT growth phase resulting from the passage of the combustion wave through the interface. Thus, $X_0$ is the interface location at the end of the RT phase, and $X$(t) is the time-dependent interface location due to shock acceleration.

Table 5.1: computation of non-reacting and reacting $\theta$ from power-law analysis using three different methods.

| $\theta$ | Regression analysis, eq(5.3) | Method of derivatives, eq. 5.4(a)-(b) | Method of initial values, eq (5.6) |
|---|---|---|---|
| Non-reacting | 0.296 | 0.290 | 0.284 |
| Reacting | 0.086 | 0.079 | 0.095 |

Table 5.1 lists estimates of the power law exponent $\theta$ determined using the methods described above for both our reacting and non-reacting simulations. From table 5.1, all three methods converge to $\theta \approx 0.29 \pm 0.006$ for the non-reacting RM flow, in general agreement with values reported from earlier simulation and experimental studies [32,67,69,70]. For instance, Youngs et al. [32]reported $\theta \approx 0.26$ (0.3) for A = 0.5 (0.9) from high-resolution numerical simulations initialized with narrowband perturbations. From impulsively accelerated experiments conducted on a Linear Electric Motor (LEM), Dimonte and Schneider reported $\theta \sim 0.24$, but with a weak dependence on the Atwood number [31]. Note that the LEM experiments experienced a short-lived RT growth, which was modeled through eq. (5.6) by taking the initial conditions $W_0^+$as the bubble/spike height at the end of this phase when the test cell had traversed a distance of $X_0$. Applying eq (5.5), Clark and Zhou [67] computed $\theta \sim 0.28$ from two sets of experiments with A = 0.22 and A = 0.48.

When a flame is present, RM growth appears to be inhibited, with lower $\theta$ values reported in table 5.1 using the different approaches outlined above. For instance, the regression analysis and the method of derivatives yield θ = 0.086 and 0.079 respectively (table 1). For third method, we employ an approach similar to [31] when evaluating θ, by taking $W_0$ = 3.37 cm as the mix width at the end of the RT expansion phase driven by the combustion wave (the corresponding distance traversed by the interface is evaluated as $X_0 = \int_0^{t_{RT}} u_{interface}(t)\, dt$ = 19.91 cm, where $t_{RT}$ signifies the end of the interface acceleration due to RT growth). During the RT-driven expansion, the mix width grows in response to a time-dependent acceleration and according to $W =$

$W_0^+\left(u_{interface}t\frac{1+C}{W_0^+}\right)^{\frac{1}{1+C}}+\frac{\beta Agt^2}{\frac{1}{1+C}\left(1+6C+\frac{1}{1+C}\right)}$, where $\beta\sim 1/2$ and $C\sim 2$ for A<<1 [31]. We attribute the lower values of growth rate in the presence of flame to increased diffusivities that result from the elevated temperatures. This is consistent with the analysis of [45] who considered the suppression of single-wavelength RM in the presence of viscous effects, and found both linear and nonlinear stages are affected (although viscous effects are less pronounced in the nonlinear stage, and are merely logarithmic for large $kh(t)$.

5.5 Molecular Mixing Fraction and Intensity of Segregation

We plot the molecular mixing fraction $\Theta$, defined according to [32] :

$$\Theta=\frac{\int_0^L<Z(1-Z)>d}{\int_0^L<Z>(1-<Z>)dx} \tag{5.7}$$

in fig. 5.4 (b) using data from our reacting and inert RM simulations. From eq. (5.7), $\Theta$ signifies the ratio of small-scale or molecular mixing to the large-scale entrainment-driven stirring, and can range from 0 (completely unmixed) to 1 (uniformly mixed). Following shock impact and ignition, the integral mixing width dramatically increases, driven by the linear stages of the RM (and variable-g RT) instabilities, while the reacting and non-reacting flows appear to produce similar levels of atomically mixed fluid at these early stages. In contrast, the nonlinear saturation of modes and onset of turbulence ($\tau > 120$) is marked by the molecular mixing fraction approaching asymptotic values of $0.926 \pm 0.001$ ($0.873 \pm 0.001$) in the reacting (non-reacting simulations). Thus, heat addition from the reaction zone boosts diffusivity resulting in increased molecular mixing across the interface. As a result, the reacting RM simulations report higher saturation values of the atomic mix fraction, relative to the corresponding inert case. The asymptotic values for $\Theta$ are in agreement with previously reported results of $\Theta\sim 0.84 \pm 0.02$ [32].

The intensity of segregation, $I$ quantifies the extent to which the scalar Z departs from the corresponding planar-averaged value <Z> and is defined as [71]

$$I = \frac{<z\prime^2>}{<Z>(1-<Z>)} \tag{5.8}$$

where, $z'$ is calculated as:

$$z' = Z - < Z >. \tag{5.9}$$

Thus, $I$ indicates the degree of inhomogeneity associated with the scalar, while $(1 - I)$ is a measure of uniformity at each plane within the mixing zone. The molecular mixing fraction $\Theta$ can be interpreted as an integral of $(1 - I)$ across the entire mixing width so that eq (5.7) can be rewritten as:

$$\Theta = 1 - \frac{\int <z\prime^2> dx}{\int <Z>(1-<Z>) dx}. \tag{5.10}$$

Figure 5.5 is a plot of the intensity of segregation as a function of <Z> for reacting and non-reacting flows at $\tau = 300$. Both cases show relatively low levels of segregation ($I < 0.16$) at this stage of flow evolution, with the lowest values observed near the midpoint of reacting mixture fraction ($I \sim 0.06$). Greater levels of segregation is observed near the edges of the mixing layer, corresponding to the contrast between mixed and unmixed fluids in these regions.

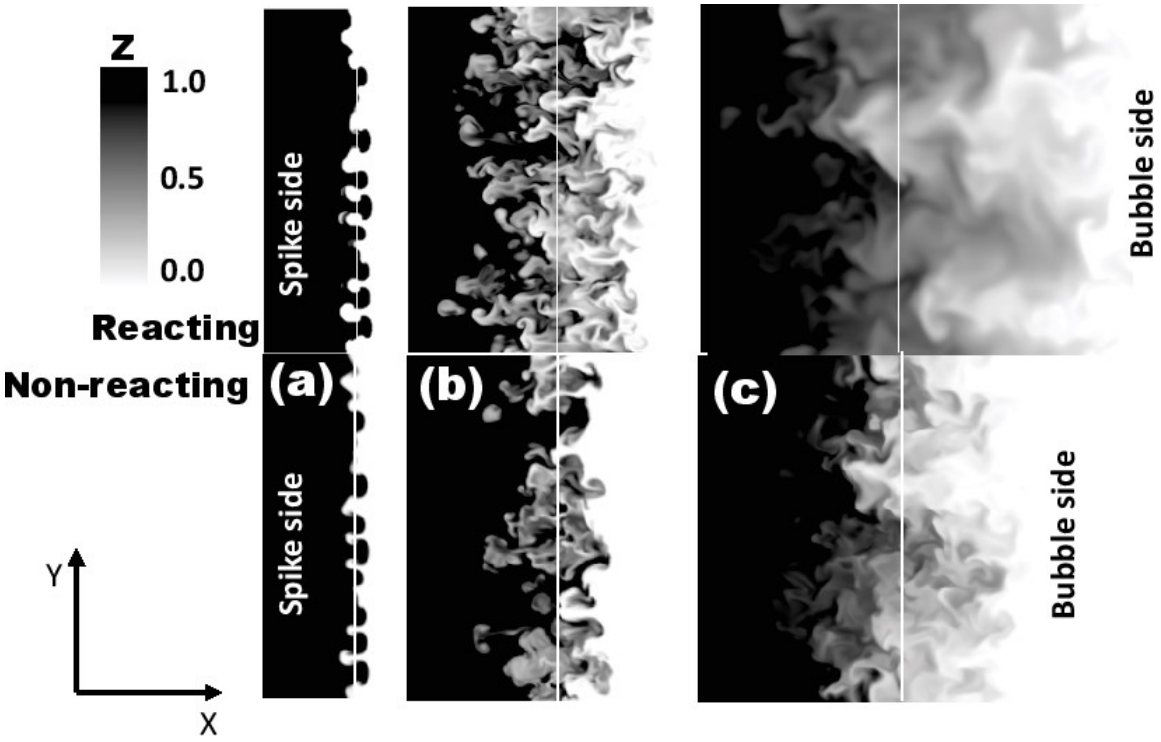


Figure 5.1: Contours of mixture fraction at the mid-plane of the shock tube showing the development of turbulent flows from reacting and non-reacting simulations at (a) $\tau \approx 2$ (b) $\tau \approx 30$ and (c) $\tau \approx 300$.

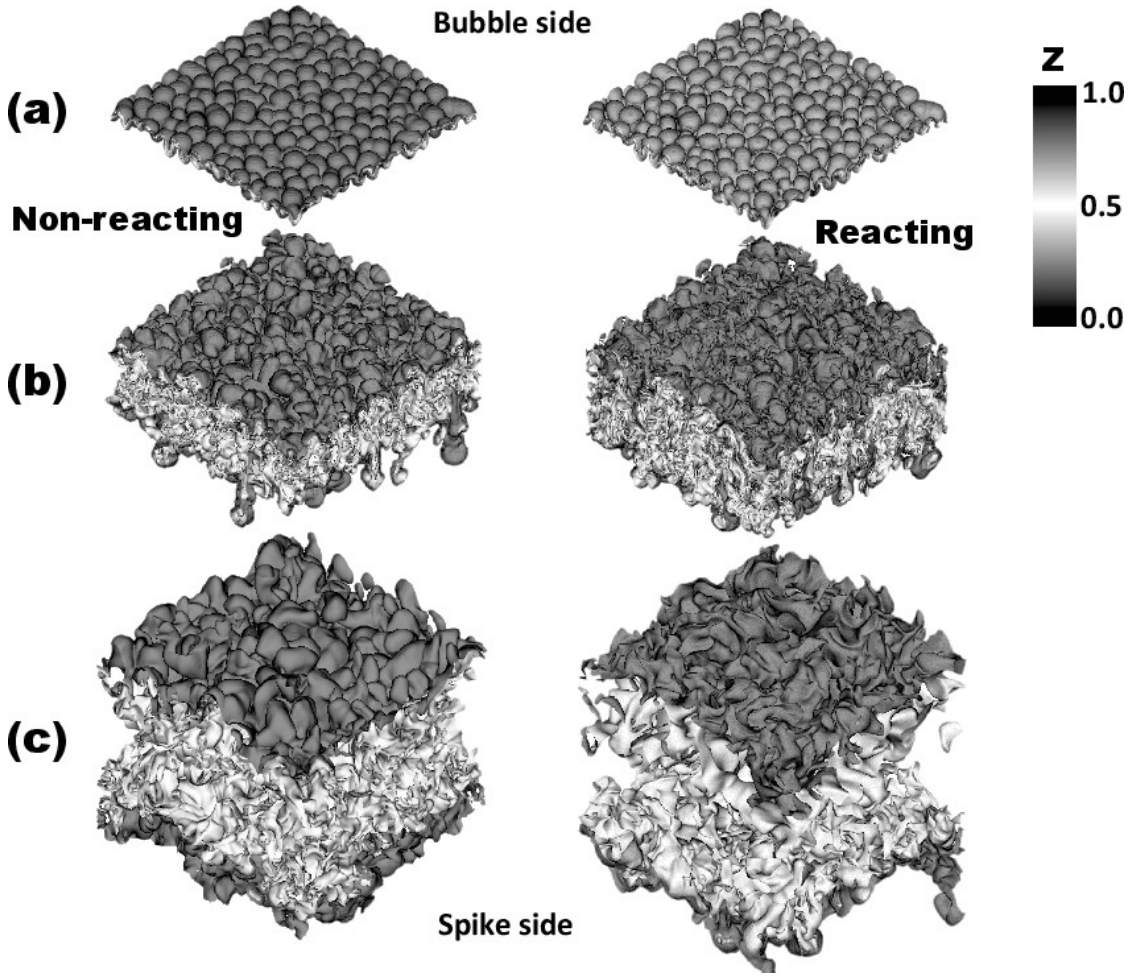


Figure 5.2: Iso-surfaces of mixture fraction Z from reacting and non-reacting simulations at (a) $\tau \approx 2$ (b) $\tau \approx 30$ and (c) $\tau \approx 300$. Dark surfaces depict iso-surfaces with Z = 0.99 (spike side) and 0.01 (bubble side)

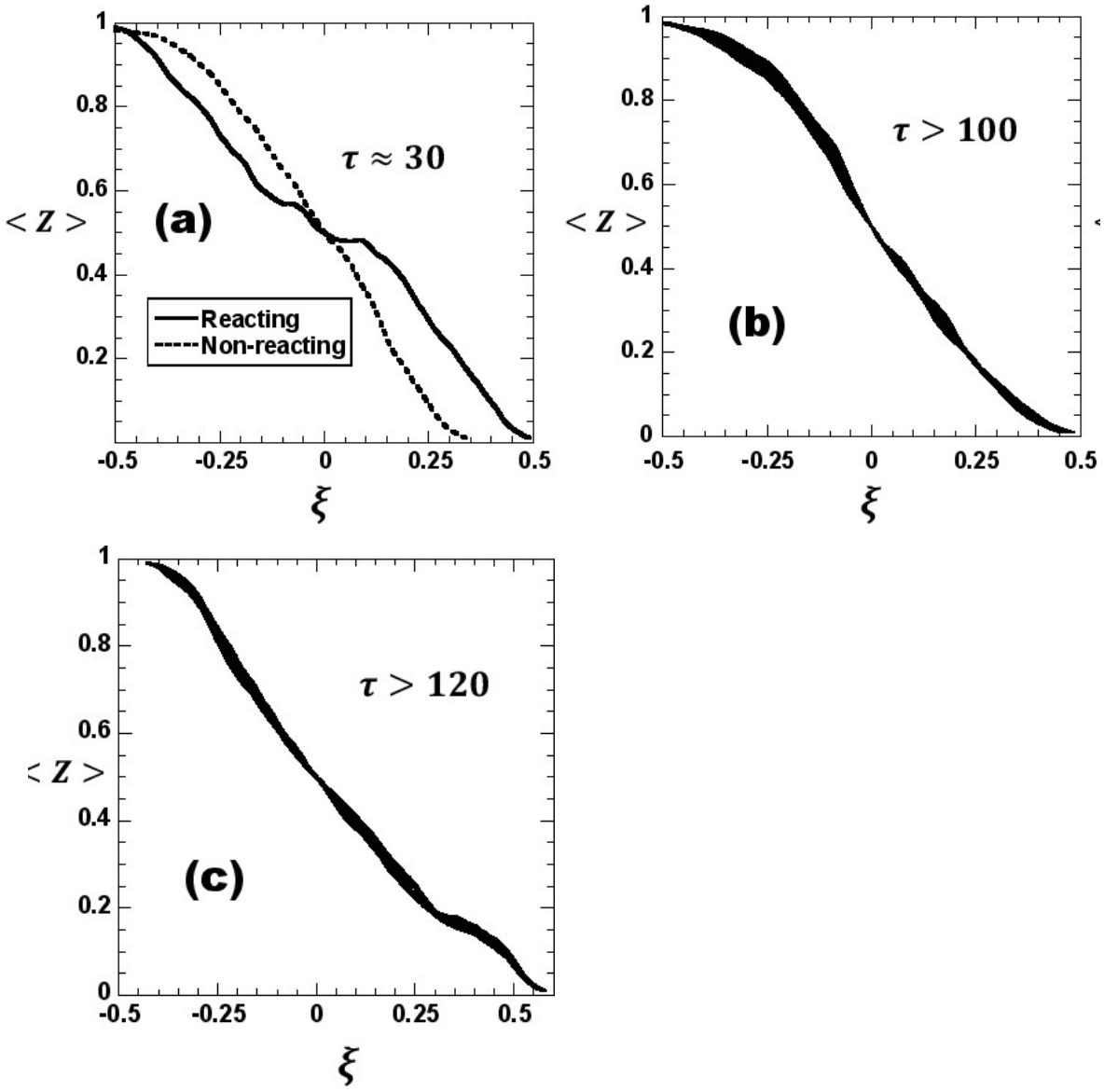


Figure 5.3: Planar-averaged mixture-fraction profiles from (a): early time (τ ~ 30), (b): non-reacting late times (τ > 100) and (c): reacting late times (τ > 120) simulations

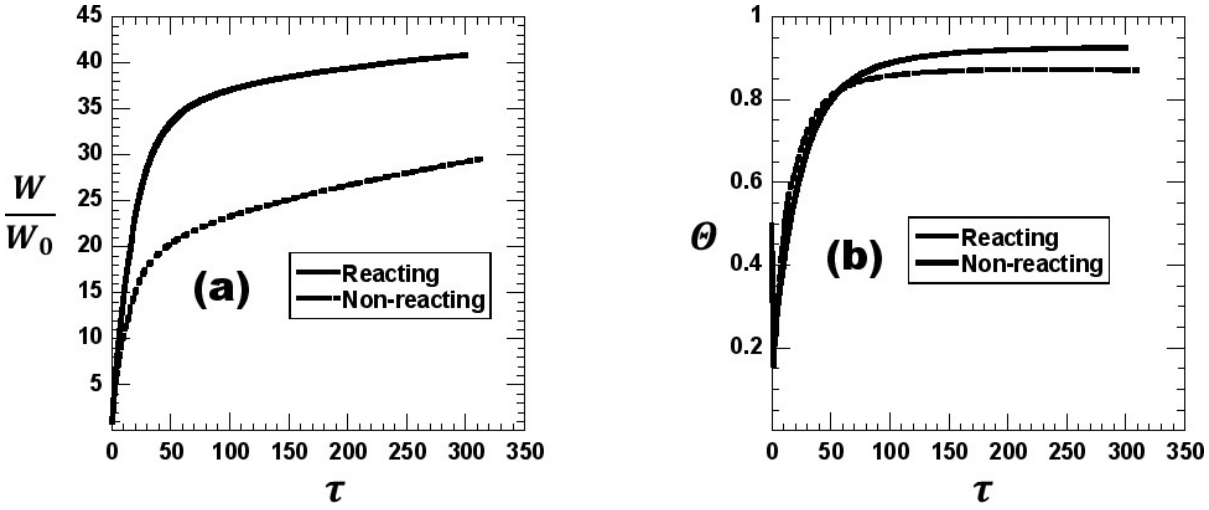


Figure 5.4: Time evolution of (a): scaled mixing width and (b): molecular mixing fraction from reacting and non-reacting simulations using FLASH.

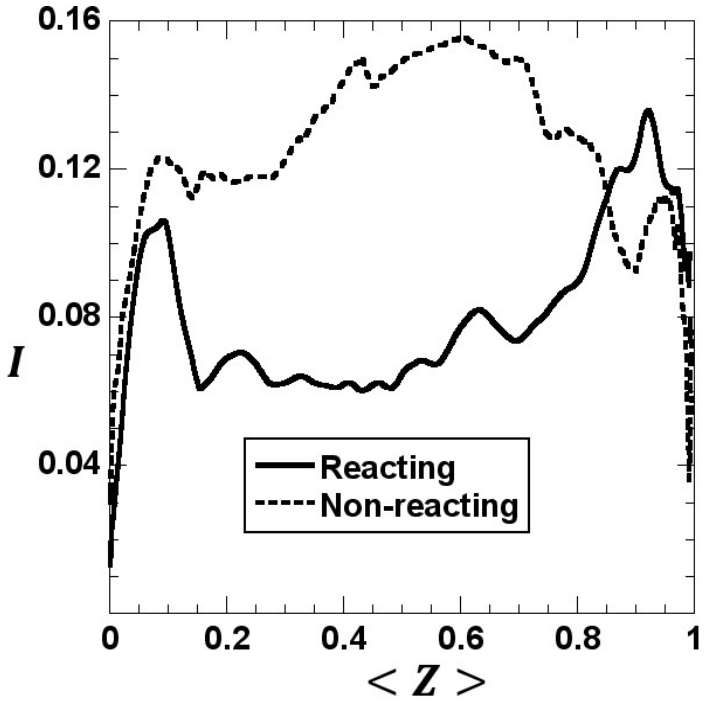


Figure 5.5: Intensity of segregation as a function of planar average of mixture fraction at $\tau = 300$ in reacting and non-reacting simulations using FLASH.

# CHAPTER 6: RMI DRIVEN FLAME STRUCTURE, FLOW/FLAME COUPLING AND MODELS

## 6.1 Scalar Dissipation Rate and Reaction Progress

In this section, we discuss the evolution of the scalar dissipation rate $\chi$ in a non-premixed reacting RM flow. The scalar dissipation rate characterizes the rate of mixing between fuel and oxidizer at the molecular level and is defined as[72-74]

$$\chi = 2D(\nabla Z)^2 \tag{6.1}$$

where $\nabla Z$ represents the spatial gradient of the scalar and D is its diffusion coefficient. In this case, the scalar is mixture fraction and D is the molecular diffusivity of mixture fraction, which is taken as the average of molecular diffusivity of species in our calculation. Thus, $\chi$ is critical to the reaction rate in non-premixed combustion, and features as an input variable in several combustion models including flamelet models [75,76], probability density function (PDF) methods [77] and conditional moment closure (CMC) [78]. Using a fast chemistry model, Bilger [73,79,80]showed the existence of a linear relationship between the turbulent reaction rate and $\chi$ in non-premixed combustion. Using one step chemical reaction between methane and air, Mastorakos et al. [81,82] concluded that, regions with lower scalar dissipation rate are prone to ignition initiation, due to lower rates of heat and scalar loss.

Figs. 6.1 (a) – (d) correspond to slices of the mixture fraction, temperature, scalar dissipation rate and concentration of OH radicals respectively, plotted on a (y-z) plane where the planar-averaged mixture fraction reaches its stoichiometric value <Z> = 0.11. The solid lines in these figures denote the intersection of the stoichiometric surface with the $(y\text{-}z)|_{<Z>=0.11}$ plane, and serve to identify surfaces with the highest likelihood of combustion. However, the actual existence of a flame at these locations depends on the level of scalar dissipation rate as well as the mixture fraction value, and can be identified through the presence of high concentrations of the OH radical (fig. 6.1-d) and enhanced temperature (fig. 6.1-b). For instance, regions of high OH concentrations occur where the stoichiometric mixture fraction iso-surfaces are highly convoluted, thus forming smaller structures. Such regions are associated with lower values of the scalar dissipation rate.. Since $\chi$ depends on the local strain rate, peaks in the scalar dissipation rate occur near mixture fraction iso-surfaces that are highly stretched. The solid lines show regions where high scalar dissipation rate limits the OH concentration and dashed lines show zones with wrinkled iso-surfaces where OH concentration is higher and scalar dissipation rate is very low. In figs. 6.1 (b) - (d), regions where the stoichiometric surfaces intersect with local peaks in $\chi$ also observe enhanced heat loss and reactant mass diffusion away from the flame front [83,84], thereby mitigating burning.

In fig. 6.2, we plot the conditional average of the scalar dissipation rate for the reacting and non-reacting simulations, defined according to $\{\chi_{st}\} \equiv \{\chi | Z = Z_{st}\}$, where the averaging is performed on the stoichiometric iso-surface.. The conditional average of $\chi$ is used to calculate the corresponding conditional probability density function of, $\boldsymbol{p(\chi_{st})}$ [72,77,85-89]. The decay observed in $\boldsymbol{\chi_{st}}$ for both the reacting and non-reacting

cases, reflects the effect of mixing in smearing spatial gradients in Z, as the flow develops from a highly segregated initial state to a well-mixed and diffuse turbulent state. Heat addition in the presence of flame, further enhances diffusive mixing so that the decay rate for $\boldsymbol{\chi_{st}}$ is sharper in this case. Interestingly, this behavior is analogous with the decay of $\{\chi_{st}\}$ with the spatial coordinate in co-flowing jet flames [90-92]. Thus, the temporal decay of $\boldsymbol{\chi_{st}}$ in a spatially homogeneous flow such as the RM problem investigated here is equivalent to the corresponding spatial decay in a temporally homogeneous flow such as the co-flowing jet.

A comparison between reacting and non-reacting $\{\chi_{st}\}$ is another noteworthy point in fig. 6.2. Early times measurements show reacting $\{\chi_{st}\}$ to be nearly considerably larger than non-reacting $\{\chi_{st}\}$. This early time enhancement can be mainly explained by amplified reacting diffusivity. Diffusivity is a strong function of temperature and rises dramatically from 0.76 $cm^2/s$ between $H_2$ and $O_2$ prior to ignition to 2.6 $cm^2/s$ shortly after the ignition. Also, according to fig. 6 (b) lower $\Theta_{\text{reacting}}$ compared to $\Theta_{\text{non-reacting}}$ indicates less mixture uniformity (and more segregation) in the reacting flow than non-reacting flow, which plays a role in increasing $(\nabla Z)^2$ and subsequently $\{\chi_{st}\}$. At late

Table 6.2: examples of $\{\chi_{st}\}$ computation in non-reacting and reacting flows at early and late-time

| Case/time | $\{D_{st}\}\ cm^2/s$ | $\{(\nabla Z)^2{}_{st}\}\ cm^{-2}$ | $\{\chi_{st}\}\ s^{-1}$ |
|---|---|---|---|
| Reacting ($\tau \approx 10$) | 3.9 | 52.96 | 410.97 |
| Non-reacting ($\tau \approx 10$) | 1.4 | 75.24 | 205.71 |
| Reacting ($\tau \approx 300$) | 4.9 | 0.69 | 6.8 |
| Non-reacting ($\tau \approx 300$) | 1.7 | 3.69 | 12.68 |

times, the spatial gradients of Z decrease due to enhanced molecular mixing imposed by the enhanced mass diffusivity. Thus, the combined effect of larger values of $D$ and dissipation of $(\nabla Z)^2$ yields lower $\{\chi_{st}\}$ in the reacting flow at late-times. Table 6.1 summarizes these parameters at early ($\tau \approx 10$) and late times ($\tau \approx 300$).

6.2 A Model for Turbulent Fluctuations of Mixture Fraction

In this section, we describe analysis to expand the scope of information about small-scale structures that can be extracted from Reynolds-averaged measurements. In particular, we utilize high-resolution numerical simulation results to examine the dependence of the variance of turbulent fluctuations of mixture fraction on turbulent flow integral quantities associated with RM mixing layer development.

We define the mean $< Z >$ and the fluctuating component of mixture fraction $z'$ as

$$Z = < Z > + z' \tag{6.2}$$

where $< \bullet >$ refers to averaging on the (y-z) plane., The fluctuating components of the mixture fraction $< z'^2 >$ can be expressed in terms of the molecular mixing fraction $\Theta$ eq (5.7) which can also be defined as eq. (6.3) given by:

$$\Theta = 1 - \frac{\int < z'^2 > d}{\int < Z > (1 - < Z >) dx} . \tag{6.3}$$

Rearranging eq. (6.3), and differentiating with respect to x, we obtain

$$< z'^2 > = (1 - \Theta) < Z > (1 - < Z >). \tag{6.4}$$

Therefore, from eq. (6.4) the turbulent fluctuations associated with the mixture fraction $< z'^2 >$ may be modeled in terms of integral quantities such as $\Theta$ and $< Z >$, that can be easily measured. We will refer to eq. (6.4) as the RM model for $< z'^2 >$. In fig. 6.3 , we compare Z-profiles of $< z'^2 >$ obtained from eq. (6.4) as well as the FLASH simulations.

The agreement between the RM model and FLASH data is within 10% across the mixing layer. However, the error increases as we approach <Z>=0 and <Z>= 1.0. This can be explained by evaluating the intensity of segregation I, at different values of <Z>. Since the RM model uses $\Theta$, it assumes a constant mixing/segregation across the mixing width. Thus, in more segregated (less mixed) regions, the RM model overestimates $< z'^2 >$ and vice versa. From fig (5.5), the fuel and oxidizer flows are more segregated near the edges of the mixing zone. Thus, in those regions, the RM model experiences greater deviation from the simulation results.

## 6.3 A Model for Mean Scalar Dissipation Rate

In many turbulent flow configurations of practical interest, the assumption of an infinitely fast chemistry is not valid, and the details of the flame/flow interaction may be relevant. For example, the reaction rates associated with regions of the flow that are at the stoichiometric mixture fraction may depend on how fast the mixture fraction field is modified by the turbulent flow. Thus, in finite-rate chemistry models that are based on the flamelet approach, the flamelet libraries are generated not only based on the distribution of the mixture fraction, but also depend on the scalar dissipation rate distribution. In this section, we extend the RM model to express the Reynolds average of $\chi$ in terms of RM-global quantities.

The Scalar dissipation rate given in eq (6.1) is the rate of decay of mixture fraction fluctuations, estimated by the variance $< z'^2 >$. Therefore, scalar dissipation rate acts on scalar fluctuations the same way that turbulent dissipation $\varepsilon$, eq (6.5) acts on fluctuations of velocity, estimated by $k$ eq (6.6):

$$< \varepsilon >= \nu \sum_{i,j} \left( < \frac{\partial u_i}{\partial x_j} + \frac{\partial u_j}{\partial x_i} > \right)^2 , i = 1,2,3 \; j = 1,2,3 \qquad (6.5)$$

$$< tke > = \frac{1}{2}\sum_i < {u_i}'^2 >, i = 1,2,3 \quad (6.6)$$

where $tke$ is the turbulent kinetic energy, $\varepsilon$ is the corresponding dissipation rate of turbulent kinetic energy [93-95], $\nu$ is kinematic viscosity and $i$ and $j$ are spatial directions. This analogy suggests that the rate of dissipation of $< z'^2 >$ by $\chi$ denoted by scalar dissipation time scale $\tau_s$, eq (6.8) is proportional to the rate of dissipation of $k$ through $\varepsilon$ denoted by turbulent dissipation time scale, $\tau_t$, eq (6.7). We can write the turbulent dissipation time scale as,

$$\tau_t = \frac{<tke>}{<\varepsilon>}. \quad (6.7)$$

Similarly, we can the write scalar dissipation time scale using

$$\tau_s = \frac{<\chi>}{<z'^2>}. \quad (6.8)$$

The expression for the mean scalar dissipation rate is often obtained based on this proportionality [96,97]. Using the relationship $\tau_t = c\tau_s$, where c is a constant, we obtain for the mean scalar dissipation rate,

$$< \chi >= c\frac{\varepsilon}{tke} < z'^2 >. \quad (6.9)$$

In eq. (6.9), $c$ is in the order of unity [72,74] and depends on several factors including the turbulent flow conditions. Model constant $c$ has been reported to lie in the range 1.5 ≤ c ≤ 3 [98], although these estimates were based on Z and $\chi$ obtained through Favre-averaging. From comparing eq. (6.9) with FLASH data, we obtain $c \approx 2.35$ within the range of previously reported values.

Combining eqs. (6.9) and (6.4), we can obtain a simple expression for $< \chi >$ entirely in terms of integral quantities associated with the RM flow:

$$< \chi > = c\frac{\varepsilon}{k} < z'^2 > \equiv c\frac{\varepsilon}{k}(1 - \Theta) < Z > (1 - < Z >). \quad (6.10)$$

Fig 6.4 compares Z-profiles of $< \chi >$ from FLASH and the RM model embodied in eq. (6.10), and shows the agreement across <Z> lies within 10%. The disagreement observed near the flame zone in fig. 5.4 is due to higher values of the turbulent energy dissipation rate $\varepsilon$ in that region, due to higher viscosity ($\sim 3.7\ cm^2/s$) near the flame compared to lower viscosity far from the flame ($\sim 0.7\ cm^2/s$) which leads to an increase in $\frac{\varepsilon}{k}$. Hence the RM model appears to overestimate $< \chi >$ in the flame neighborhood.

6.4 Ignition and Quenching

In this section, we discuss ignition, flame evolution and quenching through the behavior of the probability distribution functions of temperature in the RM flow. Fig. 6.5 (a) shows the temperature distribution on a plane with <Z> = 0.11 plotted at $\tau \approx 0$ (before shock passage), and at $\tau \approx 1$ (immediately after shock passage). Two distinctive peaks are visible at $\tau \approx 0$ corresponding to T= 300 K and T = 1000 K, and represent the initial temperatures associated with unmixed $H_2$ and $O_2$ respectively. At $\tau \approx 1$, the dominant temperature peak corresponding to $T \approx 1400$ indicates the commencement of ignition. However, from fig. 6.5 (a), it is evident the reactions have not proceeded to completion [72,99,100] since the observed temperatures are lower than the adiabatic flame temperature for $H_2$ and $O_2$ combustion (~ 3200 K). Fig 6.5-(b) shows the corresponding temperature distributions at $\tau \approx 30$ and $\tau \approx 300$. Note that the peak at $T \approx 1500$ ($\tau \approx 30$) signifies a region where the combustion reactions have not proceeded to completion. Additionally, a smaller peak is observed corresponding to the flame temperature and represents the flame region. At late-time ($\tau \approx 300$), the flame has spread significantly on the <Z> = 0.11 plane, so that the temperature distribution exhibits a sizeable peak near the flame temperature.

Figs. 6.6 (a)-(b) and 6.7 (a)-(b) depict the effect of the scalar dissipation rate on promoting or quenching the flame [83,101-103]. In fig. 6.6 (a)-(b), we show the concentration of OH as a function of the mixture fraction computed on the plane with <Z> = 0.11 at times $\tau \approx 1$, $\tau \approx 30$ and $\tau \approx 300$. Following the shock interaction (fig 6.6 (a)), the OH concentration peaks near $\chi \approx 1000$ K. At this stage of evolution, the gradients of the mixture fraction are sharp, so that the mixing zone experiences high values of scalar dissipation rate. As a result, the presence of OH molecules are more likely, due to transport by the turbulent flow field, rather than from a complete combustion process. The distribution of OH molecules at $\tau \approx 30$ in fig 6.6 (a) shows a distinct maximum at $\chi < 100\ s^{-1}$, followed by a sharp drop for $\chi > 100\ s^{-1}$. Hence, the results suggest that for $\chi > 100\ s^{-1}$, the turbulent flow does not allow adequate time for the reaction to complete, causing the flame to extinguish at $\chi > 100\ s^{-1}$. For the reacting RM flow, we define the Damkohler number as

$$Da = \frac{\tau_f}{\tau_c}, \tag{6.11}$$

where $\tau_f = \frac{1}{\chi_{st}}$ is the flow or mixing time scale and $\tau_c$ is the chemical reaction time scale. $\tau_c$ can be taken as the time required for a complete reaction and is $\sim 2.4\ e-4\ s$ in our simulation. Therefore, from figs. 6.6-(a)-(b), the RM flame tends to show local extinction zones at regions with $Da \sim < \left(\frac{0.01}{0.00024}\right) \sim 4$.

Fig. 6.7 shows evolution of probability of existence of unignited or quenched cells on the plane with <Z>=0.11. These cells are marked as cells with temperatures lower than 3000 K. Then, we calculate the probability of having an unignited or quenched cell $p(T < 3000K)$ as:

$$p(T < 3000K) \equiv \frac{Number\ of\ cell\ with\ T<3000K\ on\ the\ plane<Z>=0.11}{Total\ number\ of\ cell\ on\ the\ plane<Z>=0.11}. \quad (6.12)$$

A sharp drop in $p(T < 3000K)$ can be observed during the non-linear stage of mixing in the flow as it decreases from 0.98 at $\tau \approx 10$ to 0.68 at $\tau \approx 120$. At the onset of fully turbulent flow at $\tau > 120$, $p(T < 3000K)$ continues to decline at a lower rate and appears to approach an asymptotic value of 0.64 at late-times, fig 6.7. This decreasing behavior in the number of unignited/quenched cells is consistent can be explained by recalling. In fig 4.2 for instance, the Reynolds number drops from $\sim 22500$ at $\tau \approx 10$ to $\sim 1600$ at $\tau \approx 120$. This reduction in Re is accompanied by a reduction of turbulent intensity. Similarly, in fig 5.2 the scalar dissipation rate is reduced from $\sim 10^3$ at early-times to $\sim 10^1$ at $\tau \approx 120$, indicating a decrease in turbulent mixing and the turbulent time scales of the flow. These findings indicate that, although some level of mixing is essential to turbulent non-premixed combustion, lower rates of mixing and smaller turbulent mixing time scales allow reactions to reach completion and promote combustion.

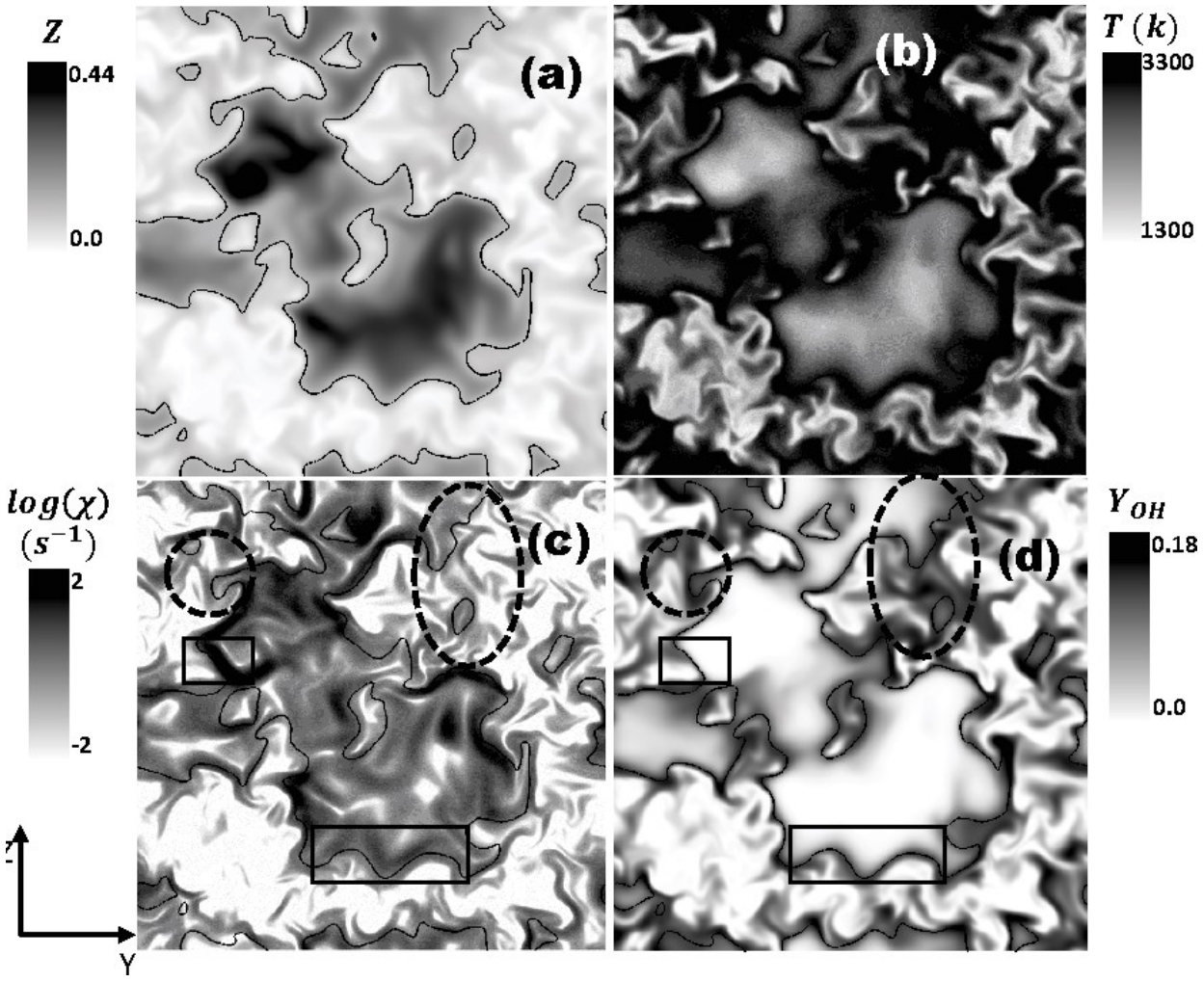


Figure 6.1 : Sliced view of (a): mixture fraction (b): Temperature, (c): scalar dissipation rate and (d): OH concentration on the plane of <Z> = 0.11. Solid lines show Z=0.11

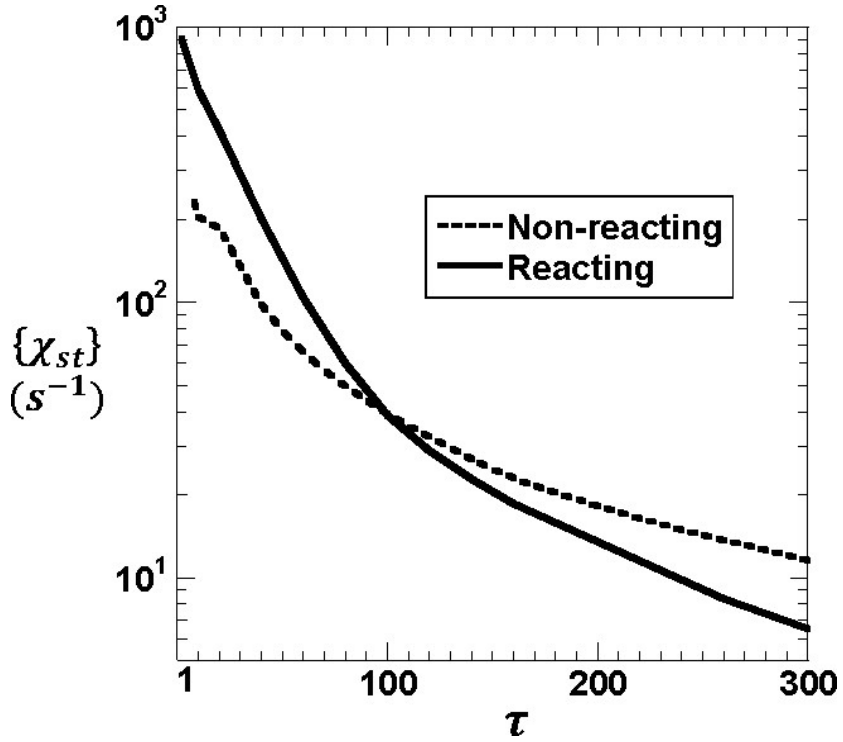


Figure 6.2: Time evolution of the conditional mean scalar dissipation rate in reacting and non-reacting flows.

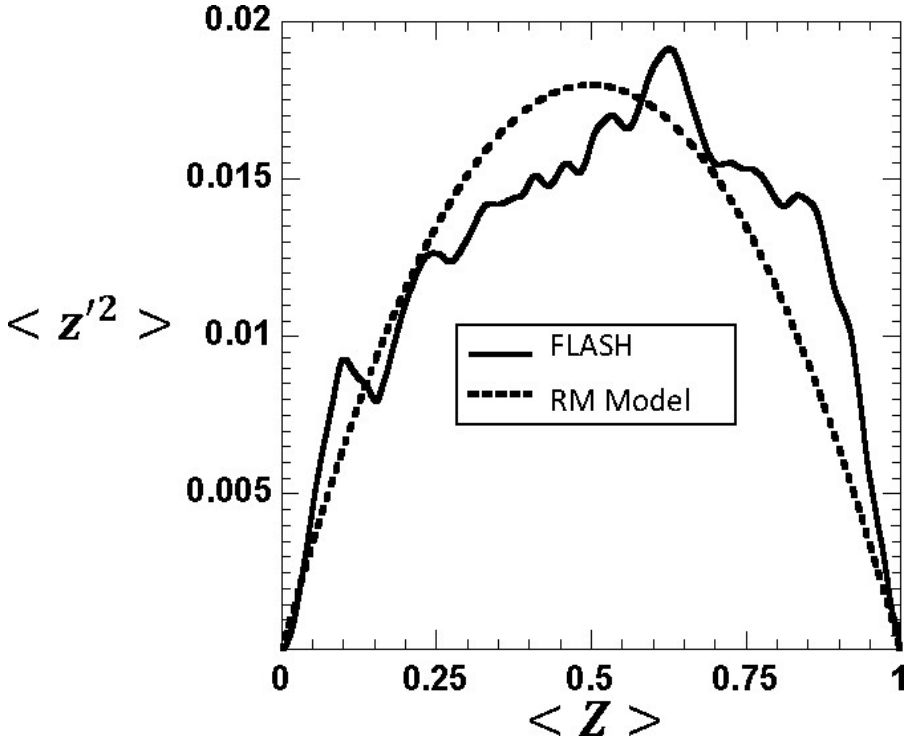


Figure 6.3: Profile of $< z'^2 >$ from FLASH simulations and the RM model as a function of <Z> at $\tau = 300$ .

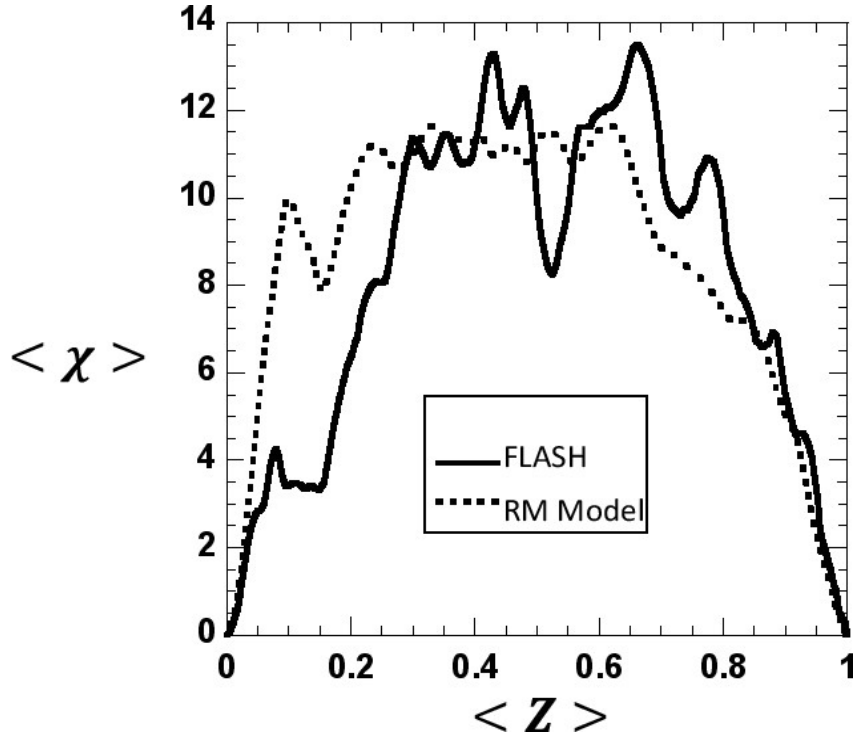


Figure 6.4: Profile of$< \chi >$ from FLASH simulations and the RM model as a function of <Z> at $\tau = 300$

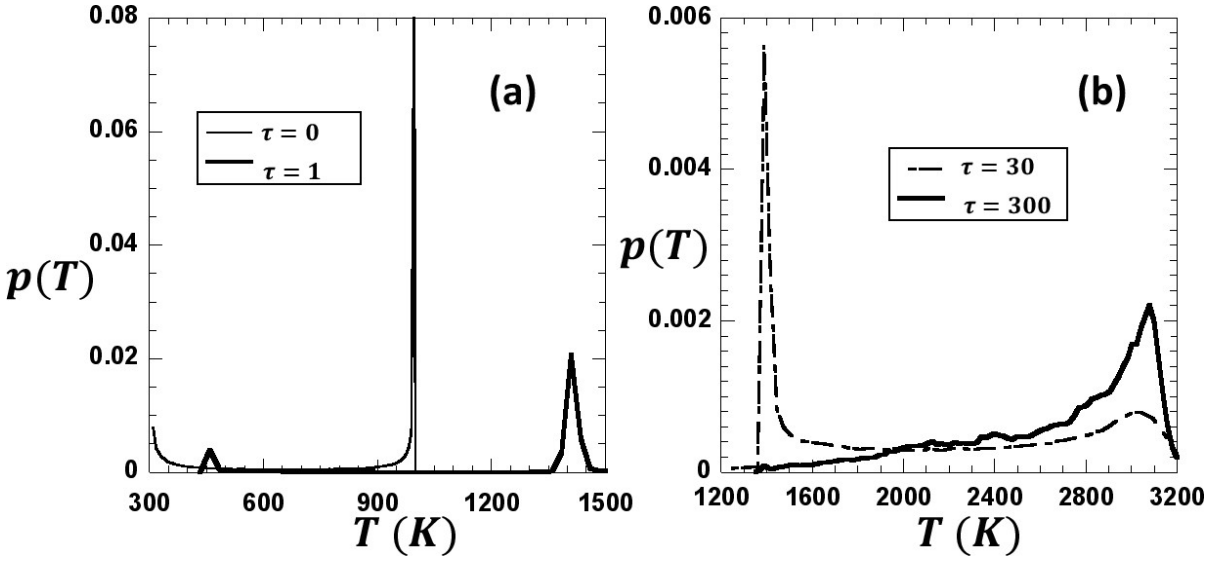


Figure 6.5: Probability distribution function of Temperature on the plane <Z> = 0.11 at (a) $\tau = 0$ and $\tau = 1$ and (b) $\tau = 30$ and $\tau = 300$.

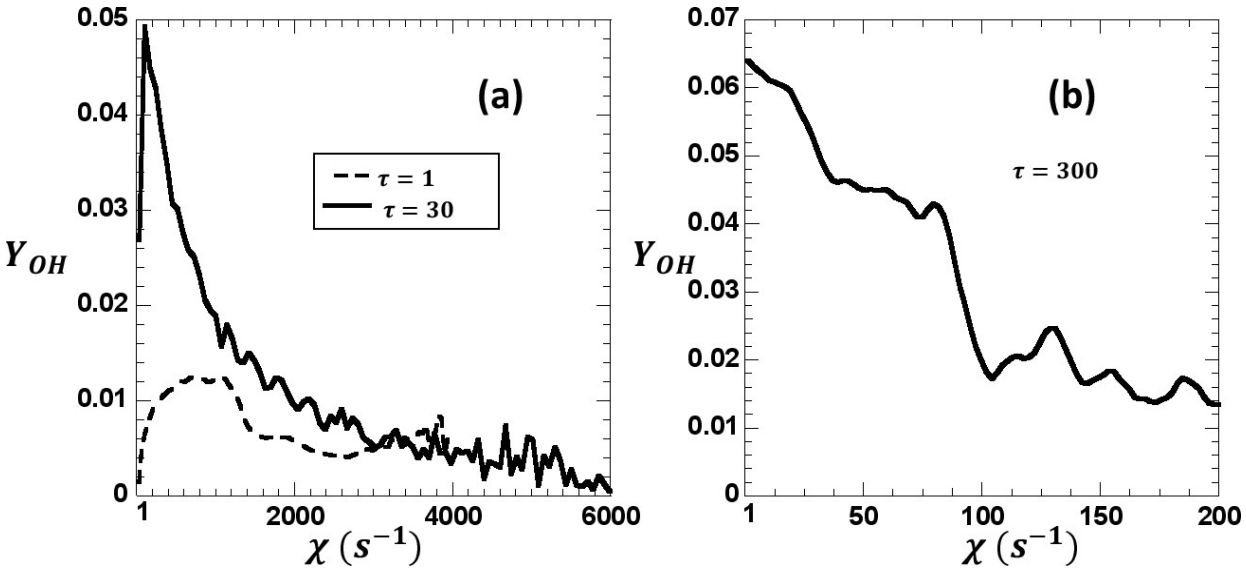


Figure 6.6: Profiles of OH concentration ($Y_{OH}$) as a function of the scalar dissipation rate $\chi$ on the plane <Z> = 0.11 at (a) $\tau = 1$ and $\tau = 30$ and (b) $\tau = 300$.

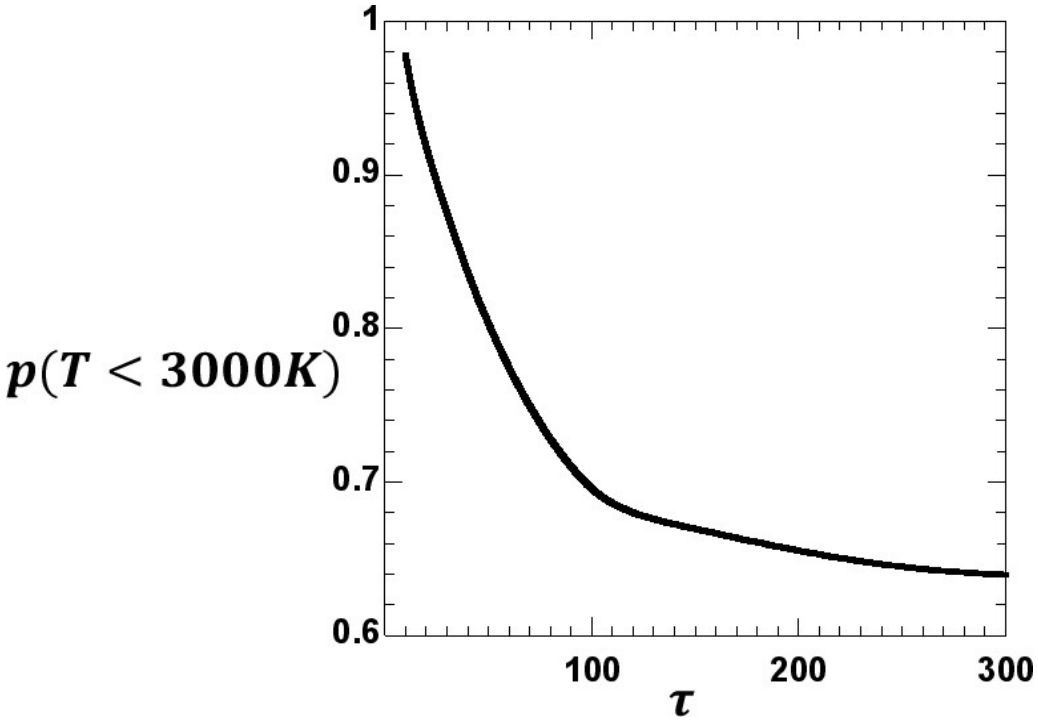


Figure 6.7: Probability of existence of unignited or quenched cells ($\boldsymbol{\tau}$<3000K) on the plane of <Z> = 0.11 over time.

# CHAPTER 7: SUMMAR AND CONCLUSIONS

In this work, we defined a novel configuration for non-premixed flames, where a Mach 1.58 shock wave passes through the interface between fuel (hydrogen) and oxidizer (oxygen). The misalignment between the pressure gradient and density gradient deposits baroclinic vorticity on the fuel/oxidizer interface, while perturbations present at the interface evolve through the Richtmyer Meshkov Instability (RMI). The resultant mixing accompanied by the shock heating ignites the local mixture, leading to the formation of a non-premixed flame.

The problem was investigated numerically using the astrophysical FLASH code, which utilizes the Piecewise Parabolic Method for advection, while a detailed model with 9 species and 19 steps was used to capture the reaction chemistry. Viscosity and thermal diffusivity of the mixture were calculated as functions of the species concentration and temperature through detailed models (eq. (2.9) - eq. (2.14)). Mass diffusivity is then obtained through the assumption of a Lewis number of ~1. The numerical resolution employed is sufficient to capture the Kolmogorov length scale at late times.

Power-law analysis: Both reacting and non-reacting RMI driven turbulent flows exhibit self-similar behavior at late times. We characterize the self-similar growth of the mixing layer using a power law form $W = A(t - t_0)^{\theta}$. The non-reacting RMI mixing

width was found to evolve with $\theta \sim 0.29$, in agreement with previously reported values [32,67,70]. In the reacting case, ignition is followed by a sudden increase in temperature, with an accompanying decrease in density. Pressure waves from ignition drive a variable-g RT instability that expands the mixing zone, and affects the growth of the mixing layer. Thus, at early times the reacting mixing width experiences a considerable enhancement compared to its non-reacting counterpart. Eventually, the higher temperatures increase the diffusivity of the mixing layer, so that the late time growth rates are suppressed relative to the inert case. Our simulations show that reacting mixing width appears to grow with $\theta \sim 0.09$ at late times.

In non-premixed combustion with infinitely fast chemistry, the entire flame structure can be calculated based on the mixture fraction distribution. This distribution is usually modeled based on the mean mixture fraction (which can be easily measured or estimated), and from the variance of the mixture fraction fluctuations (which are not readily available through modeling or measurements). In this study, we proposed a model to estimate variance of mixture fraction fluctuations using RM integral quantities such as mean of the mixture fraction and the molecular mixing parameter, which would be easy to measure in experiments.. The so-called RM model for mixture fraction fluctuations $< z'^2 >$ was validated with results from high resolution FLASH simulation. It is shown that the predicted $< z'^2 >$ from the RM model is in agreement with values from FLASH to within 10% away from the edges of the mixing layer.

When the flame dynamics are governed by finite rate chemistry, flow/flame interactions play an important role in defining the flame structure. Indeed in such situations, flame properties also depend on the scalar dissipation rate. Thus, we extend

our proposed RM model for $< z'^2 >$ to estimate the mean value of the scalar dissipation rate $< \chi >$. We apply a commonly used analogy in turbulent mixing that relates the turbulent kinetic energy dissipation rate to the scalar dissipation rate. Our results show agreement between the RM model for $< \chi >$ and the FLASH simulation data. However, the model loses accuracy near the flame, due to considerably enhanced viscosity.

Finally, we discuss the effect of shock passage and high Reynolds flows on ignition and quenching in shock driven non-premixed combustion. Our findings show that following shock incidence, during the linear and non-linear stages of mixing, the flame sheet experiences additional quenching. At this stage of the flow, the large initial Reynolds numbers (~ $10^4$) and scalar dissipation rate (~ $10^2$) prevent ignition from spreading. As a result, unignited zones are observed at the stoichiometric sheet. On the onset of fully turbulent mixing, both the Reynolds number and the scalar dissipation rate experience significant reduction. These effects increase the Damkohler number and allow additional regions on the flame sheet to reach complete combustion.

# REFERENCES

[1] R. D. Richtmyer, Communications on Pure and Applied Mathematics **13**, 297 (1960).

[2] E. Meshkov, Fluid Dynamics **4**, 101 (1969).

[3] M. Brouillette, Annual Review of Fluid Mechanics **34**, 445 (2002).

[4] N. J. Zabusky, Annual Review of Fluid Mechanics **31**, 495 (1999).

[5] S. Zhang, G. Peng, and N. Zabusky, Journal of Turbulence, N3 (2005).

[6] J. Picone and J. Boris, Journal of Fluid Mechanics **189**, 23 (1988).

[7] J. G. Wouchuk and K. Nishihara, Physics of Plasmas (1994-present) **4**, 1028 (1997).

[8] S.-I. Sohn, Physical Review E **67**, 026301 (2003).

[9] V. Goncharov, Physical review letters **88**, 134502 (2002).

[10] B. Thornber and D. Drikakis, AIAA journal **46**, 2634 (2008).

[11] J. D. Lindl, *Inertial confinement fusion: the quest for ignition and energy gain using indirect drive* (American Institute Of Physics, 1998).

[12] J. Yang, T. Kubota, and E. E. Zukoski, AIAA journal **31**, 854 (1993).

[13] P. E. Dimotakis, Annu. Rev. Fluid Mech. **37**, 329 (2005).

[14] G. H. Markstein, *Nonsteady flame propagation: AGARDograph* (Elsevier, 2014), Vol. 75.

[15] M. Gui, B. Fan, G. Dong, and J. Ye, Shock Waves **18**, 487 (2009).

[16] Y. Ju, A. Shimano, and O. Inoue, in *Symposium (International) on Combustion* (Elsevier, 1998), pp. 735.

[17] T. Jarymowycz, V. Yang, and K. Kuo, Journal of Propulsion and Power **8**, 346 (1992).

[18] G. Batley, A. McIntosh, and J. Brindley, in *Proceedings of the Royal Society of London A: Mathematical, Physical and Engineering Sciences* (The Royal Society, 1996), pp. 199.

[19] H. Teng, Z. Jiang, and Z. Hu, Acta Mechanica Sinica **23**, 343 (2007).

[20] N. Haehn, D. Ranjan, C. Weber, J. Oakley, D. Rothamer, and R. Bonazza, Combustion and Flame **159**, 1339 (2012).

[21] A. M. Khokhlov, E. S. Oran, A. Y. Chtchelkanova, and J. C. Wheeler, Combustion and Flame **117**, 99 (1999).

[22] D. Ranjan, J. Niederhaus, B. Motl, M. Anderson, J. Oakley, and R. Bonazza, Physical review letters **98**, 024502 (2007).

[23] B. Balakumar, G. Orlicz, C. Tomkins, and K. Prestridge, Physica Scripta **2008**, 014013 (2008).

[24] W. D. Arnett, The Astrophysical Journal **319**, 136 (1987).

[25] B. Collins and J. W. Jacobs, Journal of Fluid Mechanics **464**, 113 (2002).

[26] C. Tomkins, S. Kumar, G. Orlicz, and K. Prestridge, Journal of Fluid Mechanics **611**, 131 (2008).

[27] G. Dimonte, Physical Review E **69**, 056305 (2004).

[28] P. Ramaprabhu, G. Dimonte, and M. Andrews, Journal of Fluid Mechanics **536**, 285 (2005).

[29] G. Dimonte, P. Ramaprabhu, and M. Andrews, Physical Review E **76**, 046313 (2007).

[30] P. Ramaprabhu, V. Karkhanis, R. Banerjee, H. Varshochi, M. Khan, and A. Lawrie, Physical Review E **93**, 013118 (2016).

[31] G. Dimonte and M. Schneider, PHYSICS OF FLUIDS **12**, 304 (2000).

[32] B. Thornber, D. Drikakis, D. Youngs, and R. Williams, Journal of Fluid Mechanics **654**, 99 (2010).

[33] A. S. C. FLASH, *Flash user's guide* (University of Chicago, Chicago, 2014).

[34] B. Fryxell *et al.*, The Astrophysical Journal Supplement Series **131**, 273 (2000).

[35] N. Attal, P. Ramaprabhu, J. Hossain, V. Karkhanis, M. Uddin, J. R. Gord, and S. Roy, Comput. Fluids **107**, 59 (2015).

[36] P. Colella and P. R. Woodward, Journal of Computational Physics **54**, 174 (1984).

[37] S. K. Godunov, Matematicheskii Sbornik **89**, 271 (1959).

[38] G. P. Smith *et al.*, URL: http://www.me.berkeley.edu/gri_mech (1999).

[39] C. Wilke, The Journal of Chemical Physics **18**, 517 (1950).

[40] B. J. McBride, S. Gordon, and M. A. Reno, Nasa Technical Memorandum **4513** (1993).

[41] G. Billet, Journal of Computational Physics **204**, 319 (2005).

[42] X. Zhou, G. Brenner, T. Weber, and F. Durst, International journal of heat and mass transfer **42**, 1757 (1999).

[43] G. Bader and P. Deuflhard, Numerische Mathematik **41**, 373 (1983).

[44] I. S. Duff, A. M. Erisman, and J. K. Reid, *Direct methods for sparse matrices* (Clarendon Press Oxford, 1986).

[45] K. O. Mikaelian, PHYSICS OF FLUIDS **6**, 356 (1994).

[46] R. Bilger, in *Symposium (International) on Combustion* (Elsevier, 1989), pp. 475.

[47] G. Dimonte *et al.*, Physics of Fluids **16**, 1668 (2004).

[48] N. Attal and P. Ramaprabhu, in *29th International Symposium on Shock Waves 2* (Springer, 2015), pp. 1113.

[49] G. Billet, V. Giovangigli, and G. de Gassowski, Combustion Theory and Modelling **12**, 221 (2008).

[50] S. Mathur, P. Tondon, and S. Saxena, Molecular physics **12**, 569 (1967).

[51] J. Doom and K. Mahesh, Combustion and Flame **156**, 813 (2009).

[52] CERFACS, URL: http://elearning.cerfacs.fr/combustion/tools/adiabaticflametemperature/index.php (2012).

[53] D. H. Sharp, Physica D: Nonlinear Phenomena **12**, 3 (1984).

[54] G. Dimonte and M. Schneider, Physical Review E **54**, 3740 (1996).

[55] C. Kuranz *et al.*, The Astrophysical Journal **696**, 749 (2009).

[56] C. R. Weber, N. S. Haehn, J. G. Oakley, D. A. Rothamer, and R. Bonazza, Journal of Fluid Mechanics **748**, 457 (2014).

[57] B. J. Olson and J. A. Greenough, Physics of Fluids (1994-present) **26**, 101702 (2014).

[58] A. Glezer, Physics of Fluids (1958-1988) **31**, 3532 (1988).

[59] C. Weber, B. Motl, J. Oakley, M. Anderson, and R. Bonazza, Fusion Science and Technology **56**, 460 (2009).

[60] C. Tomkins, B. Balakumar, G. Orlicz, K. Prestridge, and J. Ristorcelli, Journal of Fluid Mechanics **735**, 288 (2013).

[61] C. Weber, N. Haehn, J. Oakley, D. Rothamer, and R. Bonazza, Physics of Fluids (1994-present) **24**, 074105 (2012).

[62] C. Moore, Journal of Fluid Mechanics **80**, 321 (1977).

[63] D. R. Boldman and P. F. Brinich, AIAA Journal **14**, 1656 (1976).

[64] G. P. Sutton and O. Biblarz, *Rocket propulsion elements* (John Wiley & Sons, 2010).

[65] D. L. Youngs, Laser and particle beams **12**, 725 (1994).

[66] S. Dalziel, P. Linden, and D. Youngs, Journal of Fluid Mechanics **399**, 1 (1999).

[67] T. T. Clark and Y. Zhou, Journal of applied mechanics **73**, 461 (2006).

[68] P. Ramaprabhu and M. Andrews, Journal of Fluid Mechanics **502**, 233 (2004).

[69] D. L. Youngs, in *Proceedings of the International Workshop on the Physics of Compressible Turbulent Mixing*2004), p. 392412.

[70] A. W. Cook and Y. Zhou, Physical Review E **66**, 026312 (2002).

[71] P. Danckwerts, Applied Scientific Research, Section A **3**, 279 (1952).

[72] T. Poinsot and D. Veynante, *Theoretical and numerical combustion* (RT Edwards Incorporated, 2005).

[73] R. Bilger, Flow, turbulence and combustion **72**, 93 (2004).

[74] D. Veynante and L. Vervisch, Progress in energy and combustion science **28**, 193 (2002).

[75] N. Peters, in *Symposium (International) on Combustion* (Elsevier, 1988), pp. 1231.

[76] N. Peters, *Turbulent combustion* (Cambridge university press, 2000).

[77] S. B. Pope, Progress in Energy and Combustion Science **11**, 119 (1985).

[78] R. Bilger, Physics of Fluids A: Fluid Dynamics (1989-1993) **5**, 436 (1993).

[79] R. Bilger, Energy Combus. Sci **1**, 87 (1976).

[80] R. Bilger, Combustion and Flame **30**, 277 (1977).

[81] E. Mastorakos, T. Baritaud, and T. Poinsot, Combustion and Flame **109**, 198 (1997).

[82] E. Mastorakos, A. P. D. CRUZ, T. Baritaud, and T. Poinsot, Combustion science and technology **125**, 243 (1997).

[83] E. R. Hawkes, R. Sankaran, J. C. Sutherland, and J. H. Chen, in *Journal of Physics: Conference Series* (IOP Publishing, 2005), p. 65.

[84] C. P. Chen, PhD, National Chen-Kung University, 2007.

[85] J. Xu and S. B. Pope, Combustion and Flame **123**, 281 (2000).

[86] J.-Y. Chen, W. Kollmann, and R. Dibble, Combustion Science and Technology **64**, 315 (1989).

[87] W. Jones and M. Kakhi, Combustion and Flame **115**, 210 (1998).

[88] A. Masri and S. Pope, Combustion and Flame **81**, 13 (1990).

[89] V. Saxena and S. B. Pope, in *Symposium (International) on Combustion* (Elsevier, 1998), pp. 1081.

[90] P. C. Babu and K. Mahesh, Physics of Fluids **16** (2004).

[91] R. L. Gordon, A. R. Masri, S. B. Pope, and G. M. Goldin, Combustion and Flame **151**, 495 (2007).

[92] N. Clemens and P. Paul, Combustion and Flame **102**, 271 (1995).

[93] S. B. Pope, (IOP Publishing, 2001).

[94] B. E. Launder and D. Spalding, Computer methods in applied mechanics and engineering **3**, 269 (1974).

[95] D. C. Wilcox, *Turbulence modeling for CFD* (DCW industries La Canada, CA, 1998), Vol. 2.

[96] Y.-S. Chen and S.-W. Kim, (1987).

[97] Z. Yang and T. Shih, AIAA journal **31**, 1191 (1993).

[98] H. Pitsch, CEFRC Combustion Summer School (2014).

[99] N. Peters, Combustion Science and Technology **30**, 1 (1983).

[100] R. R. Cao and S. B. Pope, Combustion and Flame **143**, 450 (2005).

[101] C. D. Pierce and P. Moin, Journal of Fluid Mechanics **504**, 73 (2004).

[102] T. Echekki and J. H. Chen, Combustion and Flame **134**, 169 (2003).

[103] P. Domingo and L. Vervisch, in *Symposium (International) on Combustion* (Elsevier, 1996), pp. 233.

[104] Y. Zhou, G. B. Zimmerman, and E. W. Burke, Physical Review E **65**, 056303 (2002).

[105] P. Moin and K. Mahesh, Annual review of fluid mechanics **30**, 539 (1998).

[106] R. S. Rogallo and P. Moin, Annual Review of Fluid Mechanics **16**, 99 (1984).

[107] J. Eggels, F. Unger, M. Weiss, J. Westerweel, R. Adrian, R. Friedrich, and F. Nieuwstadt, Journal of Fluid Mechanics **268**, 175 (1994).

# APPENDIX A-1: KOLMOGOROV LENGTH SCALE

In order to resolve the turbulent flow, the grid resolution has to adequately resolve the Kolmogorov length scales of the flow [61,93,104]. The Kolmogorov length scale, $\eta$ can be computed according to [93] :

$$\eta = WRe^{-\frac{3}{4}}$$

(1-A)

Note that $\eta$ can be computed *a priori* by invoking the anticipated power law behavior of W. By substituting eq (4.5) and (5.3) into eq (1-A), we get

$$\eta = \left\{ A \left(\frac{\theta}{\nu}\right)^{\frac{3}{2}} (t - t_0)^{\theta - \frac{3}{2}} \right\}^{-\frac{1}{2}}.$$

(2-A)

Fig (1-A) shows $\frac{\eta}{\Delta}$ for both reacting and non-reacting simulations as a function of time using FLASH as well as eq (2-A), where $\Delta$ is the computational grid size. Thus, results from FLASH are consistent with the exponential decay calculated using derivatives of power-law expression at late-times. From fig (1-A), a grid spacing of $\frac{6}{448}\ cm$ should resolve the Kolmogorov length scales of the reacting flow, since for $\tau >$

70 the value of $\frac{\eta}{\Delta}$ exceeds 1. In the non-reacting case, for $\tau > 230$, $\frac{\eta}{\Delta}$ asymptotically reaches 0.5.

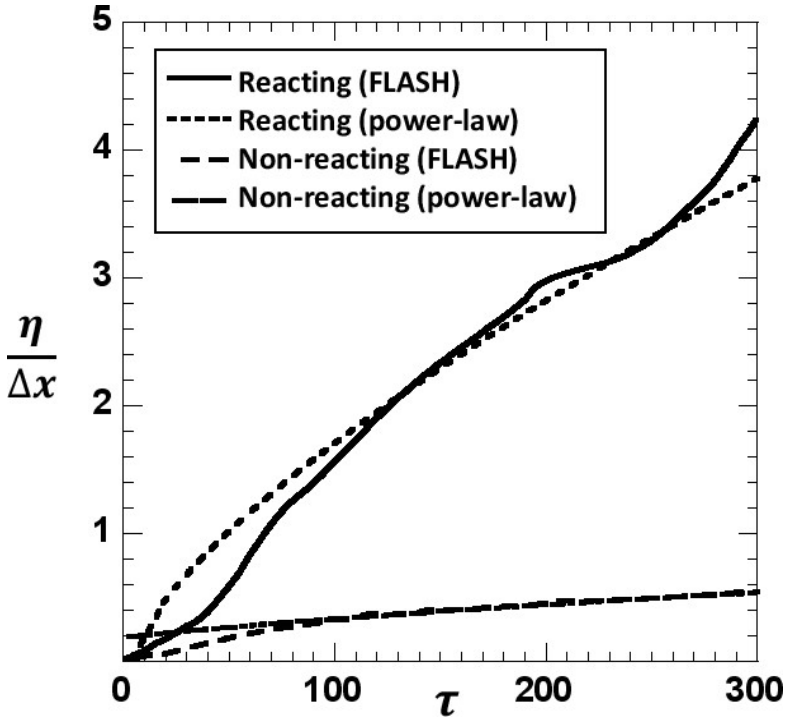


Figure 1A: Ratio of the Kolmogorov length scale to the simulation grid size for reacting and non-reacting cases as a function of turbulent flow time scale from FLASH and power-law derivatives.